Article

Structural insights into BCDX2 complex function in homologous recombination

https://doi.org/10.1038/s41586-023-06219-w

Received: 23 January 2023

Accepted: 15 May 2023

Published online: 21 June 2023

Check for updates

Yashpal Rawal[1,8], Lijia Jia[1,8], Aviv Meir[2,8], Shuo Zhou[1], Hardeep Kaur[1], Eliza A. Ruben[1], Youngho Kwon[1], Kara A. Bernstein[3], Maria Jasin[4], Alexander B. Taylor[1], Sandeep Burma[1,5], Robert Hromas[6], Alexander V. Mazin[1], Weixing Zhao[1], Daohong Zhou[1], Elizabeth V. Wasmuth[1], Eric C. Greene[2]✉, Patrick Sung[1]✉ & Shaun K. Olsen[1,7]✉

Homologous recombination (HR) fulfils a pivotal role in the repair of DNA double-strand breaks and collapsed replication forks[1]. HR depends on the products of several paralogues of *RAD51*, including the tetrameric complex of RAD51B, RAD51C, RAD51D and XRCC2 (BCDX2)[2]. BCDX2 functions as a mediator of nucleoprotein filament assembly by RAD51 and single-stranded DNA (ssDNA) during HR, but its mechanism remains undefined. Here we report cryogenic electron microscopy reconstructions of human BCDX2 in apo and ssDNA-bound states. The structures reveal how the amino-terminal domains of RAD51B, RAD51C and RAD51D participate in inter-subunit interactions that underpin complex formation and ssDNA-binding specificity. Single-molecule DNA curtain analysis yields insights into how BCDX2 enhances RAD51–ssDNA nucleoprotein filament assembly. Moreover, our cryogenic electron microscopy and functional analyses explain how RAD51C alterations found in patients with cancer[3–6] inactivate DNA binding and the HR mediator activity of BCDX2. Our findings shed light on the role of BCDX2 in HR and provide a foundation for understanding how pathogenic alterations in BCDX2 impact genome repair.

Failure to remove DNA lesions induced by environmental and endogenous agents can cause cell death or compromise genome integrity to lead to neoplastic transformation of cells[7]. DNA double-strand breaks (DSBs) are among the most deleterious of all such lesions, as a failure to eliminate them can lead to the types of gross chromosomal rearrangement found in cancer cells[8]. HR is a major DSB repair pathway that involves processing of DSB ends to generate a long 3′ ssDNA overhang that serves as the platform for the assembly of the machinery that catalyses repair[1]. The ssDNA tail is rapidly coated by replication protein A (RPA), which prevents ssDNA secondary structure formation and spurious DNA degradation. RPA is subsequently replaced by the recombinase RAD51, which assembles into a presynaptic nucleoprotein filament capable of conducting DNA homology search and strand invasion[9]. RPA–RAD51 exchange on ssDNA is facilitated by HR mediators[2,10].

Six paralogues of *RAD51* (namely, *RAD51B*, *RAD51C*, *RAD51D*, *XRCC2*, *XRCC3* and *SWSAP1*) exist in humans, and they form distinct complexes that act as mediators of RAD51 presynaptic filament assembly[2]. On the basis of sequence analysis and structure prediction, the products of these paralogues harbour a conserved ATP-binding domain, and with the exception of XRCC2 and SWSAP1, a globular N-terminal domain (NTD) of unknown function[2]. Three complexes comprising the products of paralogues of *RAD51* have been described: the tetrameric RAD51B–RAD51C–RAD51D–XRCC2 (BCDX2) complex, the dimeric RAD51C–XRCC3 (CX3) complex[11] and the dimeric SWSAP1–SWS1 complex[12]. Elimination of any BCDX2 subunit renders cells hypersensitive to DNA-damaging agents and reduces DNA-damage-induced RAD51 focus formation[5,13]. Mutations in *RAD51B*, *RAD51C* and *RAD51D* are found in patients with cancer[3–6], and mutations in *RAD51C* and *XRCC2* are associated with the cancer-prone syndrome Fanconi anaemia[14]; accordingly, these genes are also known as *FANCO*[15,16] and *FANCU*[17], respectively.

At present there is no structural information on any of the complexes comprising the products of paralogues of human *RAD51*, and how they promote RAD51 presynaptic filament assembly remains undetermined. Herein, we present high-resolution cryogenic electron microscopy (cryo-EM) reconstructions of human BCDX2 in apo and ssDNA-bound states. The structures reveal determinants of complex assembly and provide insights into the nucleotide dependence and DNA substrate specificity of BCDX2. Notably, the NTDs of BCDX2 subunits participate in extensive intermolecular interactions that underpin complex assembly and confer ssDNA specificity through steric occlusion. Our reconstructions provide the basis for understanding the structural relevance of alterations in BCDX2 subunits found in patients with cancer. Mechanistic insights are derived from biochemical and biophysical analyses, including single-molecule studies revealing how BCDX2 mediates RPA–RAD51 exchange on ssDNA. Collectively, our studies provide insights into the HR mediator function of BCDX2 and the molecular basis by which BCDX2 alterations lead to cancer, and provide the foundation for targeting BCDX2 for therapeutic intervention.

[1]Department of Biochemistry & Structural Biology and Greehey Children's Cancer Research Institute, University of Texas Health Science Center at San Antonio, San Antonio, TX, USA. [2]Department of Biochemistry and Molecular Biophysics, Columbia University Irving Medical Center, New York, NY, USA. [3]Department of Biochemistry & Biophysics, University of Pennsylvania School of Medicine, Philadelphia, PA, USA. [4]Developmental Biology Program, Memorial Sloan Kettering Cancer Center, New York, NY, USA. [5]Department of Neurosurgery, University of Texas Health Science Center at San Antonio, San Antonio, TX, USA. [6]Department of Medicine, University of Texas Health Science Center at San Antonio, San Antonio, TX, USA. [7]Glenn Biggs Institute for Alzheimer's and Neurodegenerative Diseases, San Antonio, TX, USA. [8]These authors contributed equally: Yashpal Rawal, Lijia Jia, Aviv Meir. ✉e-mail: ecg2108@cumc.columbia.edu; sungp@uthscsa.edu; olsens@uthscsa.edu

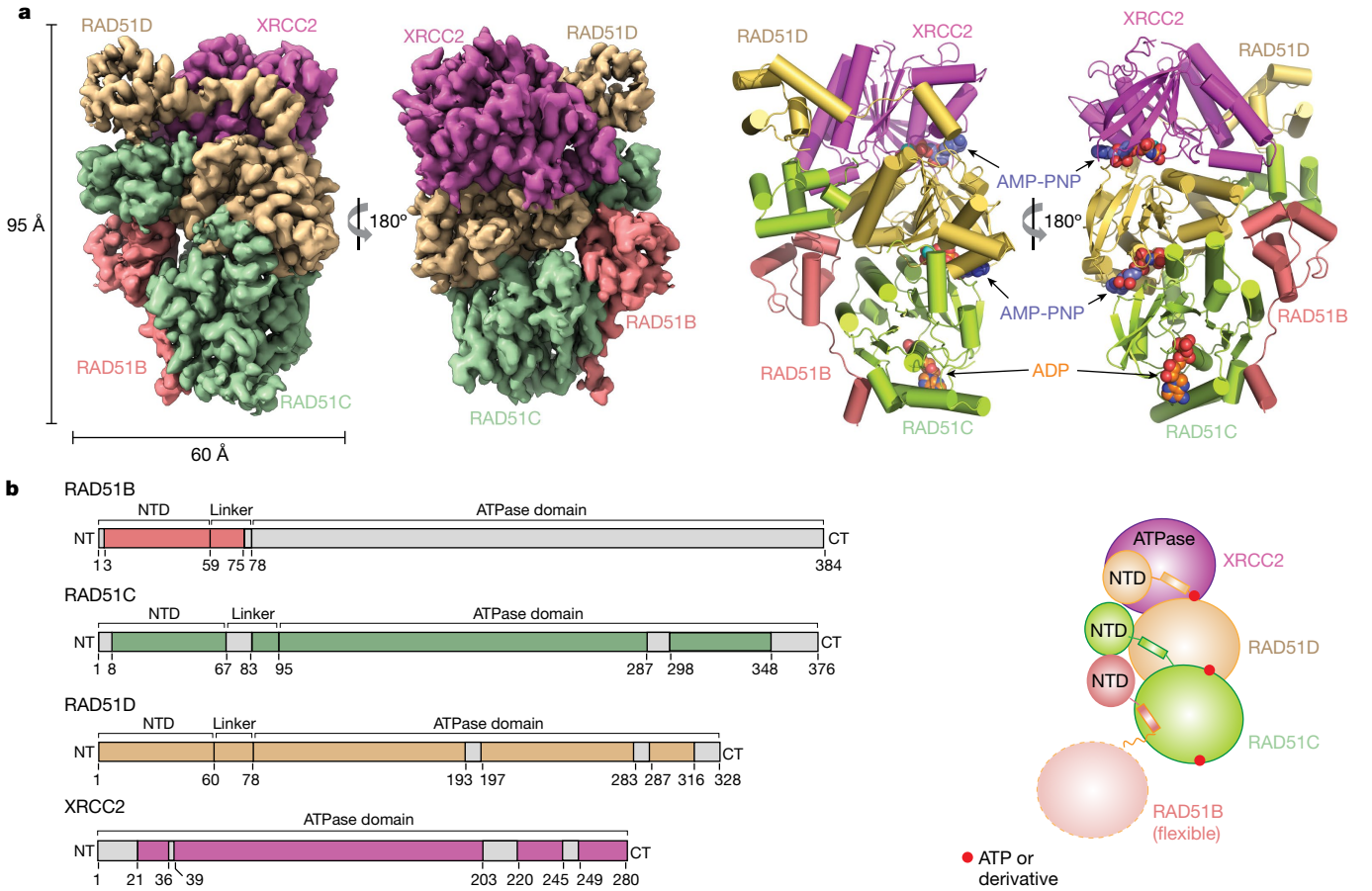


Fig. 1 | Cryo-EM structure of the BCDX2 complex. a, Left, cryo-EM maps of the BCDX2 complex assembled in the presence of AMP-PNP. Individual subunits are labelled and colour coded. Two views related by a 180° rotation about the *y*-axis are presented. Right, schematic representation of the BCDX2 complex. ADP and AMP-PNP molecules are shown as spheres. **b**, Left, schematic outlining the domain organization of BCDX2 subunits with regions of disorder in the structure indicated in grey. NT, amino terminus; CT, carboxy terminus. Right, schematic diagram highlighting the main structural features of the BCDX2 complex.

Cryo-EM structure of apo BCDX2

To gain insights into the structure and function of BCDX2, we co-expressed subunits together in insect cells and purified a stoichiometric complex to homogeneity in the presence of ATP and its cofactor Mg^{2+} (ATP/Mg^{2+}), which are required to maintain complex stability (Extended Data Fig. 1a). Analysis by mass photometry confirmed monodispersity of BCDX2 as a complex of about 150 kDa and, consistent with previous results[11], also revealed dissociation of the complex on omission of ATP/Mg^{2+} (Extended Data Fig. 1b). Unless otherwise noted, all of the assays were carried out with ATP/Mg^{2+} whereas samples subjected to cryo-EM analysis were exchanged into buffer containing AMP-PNP/Mg^{2+}. We collected high-quality cryo-EM data to generate a three-dimensional map of BCDX2 with a nominal resolution of 2.3 Å (masked) that provides detailed information regarding complex architecture and functional insights (Extended Data Figs. 1c and 2a–c and Extended Data Table 1). We refer to this structure as apo BCDX2 to distinguish it from the ssDNA-bound structure reported later. In the apo structure, RAD51D interacts on either side of its ATP-binding domain with the ATP-binding domains of RAD51C and XRCC2 (Fig. 1). The NTDs of RAD51B, RAD51C and RAD51D decorate the periphery of the complex with each NTD being in close contact with both the ATPase domain and NTD of the neighbouring subunit, and XRCC2, which lacks an NTD, associates with the ATP-binding domain of RAD51D and the NTDs of RAD51C and RAD51D (Fig. 1). There was clear nucleotide density within the ATP-binding sites of RAD51C (ADP), RAD51D (AMP-PNP) and XRCC2 (AMP-PNP; Fig. 1a and Extended Data Fig. 2d,e). The extensive network of interactions between RAD51C, RAD51D and AMP-PNP at the RAD51C–RAD51D interface (described below) probably explains the dependence of BCDX2 stability on ATP/Mg^{2+} (Extended Data Fig. 1b; ref. 6). Whereas the NTD and linker region of RAD51B are well ordered, its predicted ATP-binding domain is not visible in our cryo-EM maps (Fig. 1), probably because it is highly dynamic.

NTDs underpin a unique BCDX2 architecture

Despite sharing only 16–28% overall sequence identity[18], the ATP-binding domains and NTDs of the BCDX2 subunits and RAD51 are highly similar and superimpose well (Extended Data Table 2). The main difference between the BCDX2 subunits and RAD51 is the relative orientation of the NTDs (Fig. 2). Whereas the NTD of RAD51 folds back towards its ATPase domain at an approximately 45° angle and participates in a small network of interactions with the ATPase domain, the NTDs of RAD51C and RAD51D project away from their ATPase domains at an angle of about 90°, which prevents intramolecular contacts (Fig. 2). Thus, the NTDs within the RAD51 presynaptic filament make few contacts with neighbouring subunits (Protein Data Bank (PDB) 7EJC)[19], but the NTDs of RAD51B, RAD51C and RAD51D show extensive interactions with both the NTDs and ATPase domains of neighbouring subunits.

Although the NTDs of RAD51B, RAD51C and RAD51D project away from their ATP-binding domains (Fig. 2a, left), the NTDs themselves each adopt markedly different spatial orientations (Fig. 2a, right).

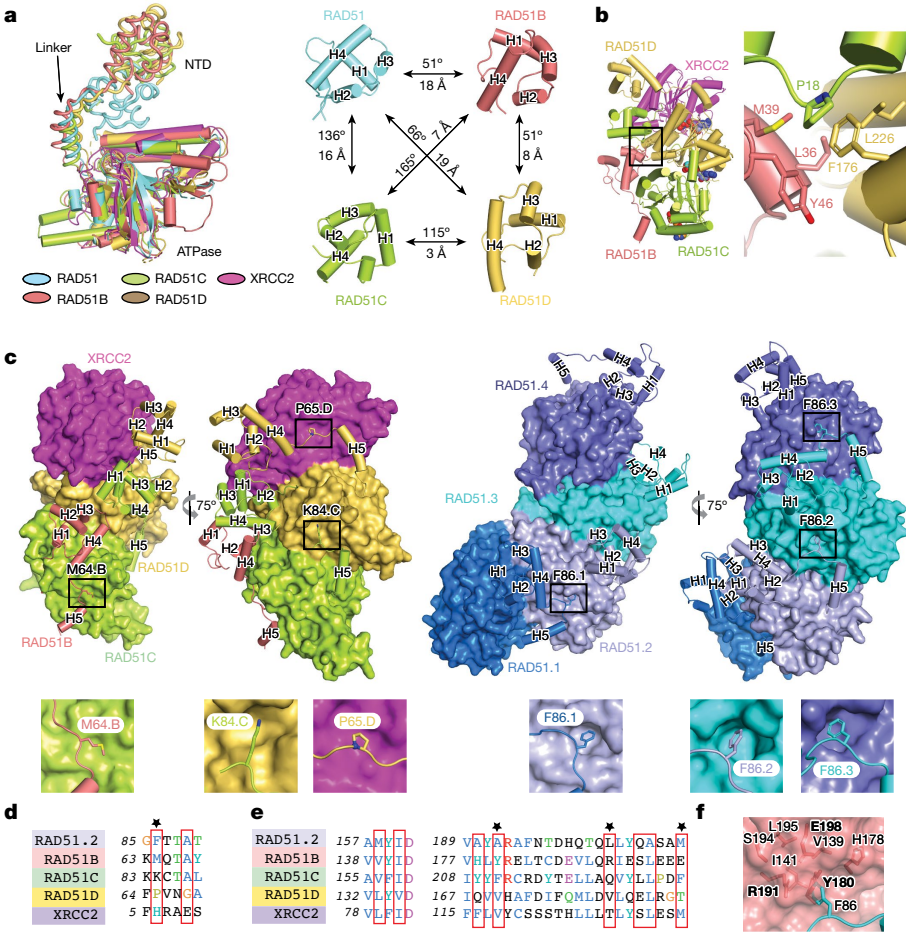


Fig. 2 | BCDX2 architecture is reinforced by a unique NTD configuration. **a**, Relative orientation of NTDs, linkers and ATPase domains of BCDX2 subunits. Left, the ATPase domains of RAD51 and BCDX2 subunits superimposed and shown as cartoon representations coloured as indicated. Linker and NTDs are shown as cartoon tubes. Right, standalone NTDs with the relative rotation and translation between NTD pairs indicated. **b**, A unique tripartite interaction between the NTDs of RAD51B and RAD51C and the ATPase domain of RAD51D. Left, an overview of the structure shown as a schematic representation; right, a magnified view of the tripartite network with interacting residues shown as sticks. **c**, Surface representations of the ATPase domains of the BCDX2 complex (two leftmost structures) and RAD51 filament (two rightmost structures; PDB 7EJC) with linker and NTDs shown as cartoon representations. Residues corresponding to the polymerization motif of RAD51 are shown as sticks, with magnified views shown underneath. The four subunits of RAD51 are distinguished by numbers 1–4 appended to the labels (RAD51.1, RAD51.2 and so on). **d**, Structure-based sequence alignment of the RAD51 polymerization motif. **e**, Structure-based sequence alignment of the RAD51 polymerization motif binding pocket (Phe86). **f**, Model of RAD51–RAD51B showing the polymerization motif pocket of RAD51B filled by bulky hydrophobic and charged residues incompatible with Phe86 binding. RAD51B is shown as a semitransparent surface (salmon) with residues corresponding to the RAD51 polymerization motif binding pocket shown as sticks. Phe86 of the RAD51 polymerization motif is shown as sticks. Residues that most strongly block the RAD51 polymerization motif binding pocket are shown in bold.

As noted above, the NTDs of RAD51B, RAD51C and RAD51D harbour a conserved structure comprising four α-helices (H1–H4), and, notably, structural comparison reveals rigid-body rotations between 51° and 165° and translations of 3 to 8 Å relative to the ATPase domains (Fig. 2a, right). As such, entirely different NTD surfaces of RAD51B, RAD51C and RAD51D are involved in intermolecular interactions within BCDX2 (Extended Data Fig. 3), revealing a prominent network of tripartite interactions involving Pro18 of the RAD51C NTD, Leu36, Met39 and Tyr46 of the RAD51B NTD and Phe176 and Leu226 from the ATPase domain of RAD51D (Fig. 2b).

RAD51 possesses an oligomerization motif spanning residues Phe86 to Ala89 (referred to as the FXXA motif)[20,21]. Specifically, the side chains of Phe86 and Ala89 insert into hydrophobic pockets on the surfaces of adjacent subunits within the RAD51 filament (Fig. 2c–e). As such, the F86E and A89E mutants of RAD51 fail to oligomerize and do not form DNA-damage-induced nuclear foci[20,22]. The products of paralogues of *RAD51* lack the FXXA motif, with Met64 in RAD51B, Lys84 in RAD51C, Pro65 in RAD51D, and His6 within the disordered N-terminal region of XRCC2 replacing Phe86 of RAD51 (Fig. 2c–e). Notably, regions of BCDX2 subunits corresponding to the hydrophobic pocket that accommodates Phe86 within the RAD51 presynaptic filament are almost completely filled by bulkier hydrophobic and charged side chains (Fig. 2e,f). Our structural analysis reveals crucial differences that underpin the oligomeric structure of BCDX2 in relation to the RAD51 filament.

BCDX2 ATPase sites

A Mg^{2+}-coordinated AMP-PNP molecule is observed at the interface between XRCC2 and RAD51D in the XRCC2 active site and another at the interface between RAD51D and RAD51C in the RAD51D active site (Extended Data Fig. 4a). The AMP-PNP molecules are nearly completely buried at these conserved interfaces, with about 83% of total accessible surface area being occluded from solvent. The adenine of AMP-PNP is sandwiched by Glu56 and Arg91 of XRCC2 and Pro302 in RAD51D (Extended Data Fig. 4a,b). A similar arrangement is observed for AMP-PNP bound by RAD51D with Gln115 and Arg145 of RAD51D and

Lys333 of RAD51C sandwiching the adenine (Extended Data Fig. 4a,b). Overall, these AMP-PNP contacts closely resemble those observed for the ATPase site of RAD51 (ref. 19,23,24). Backbone amide groups of P-loop residues and Mg^{2+} interact with the β-phosphate of AMP-PNP bound to both the RAD51D and XRCC2 active sites. A conserved and mechanistically important network of contacts is observed between the γ-phosphate of AMP-PNP and lysine residues from the ATP-binding site (Lys113 in RAD51D and Lys54 in XRCC2), lysine residues from adjoining subunits that contact ATP in *trans* (Lys328 in RAD51C and Lys297 of RAD51D) and Mg^{2+} (Extended Data Fig. 4a,b). The two Mg^{2+} ions are coordinated by conserved threonine residues within the Walker A motif (Thr114 in RAD51D and Thr52 in XRCC2; Extended Data Fig. 4a,b).

The constellation of amino acids within the active sites of XRCC2 and RAD51D are conserved within RAD51C, but a key difference is that there are no *trans* contacts to the nucleotide owing to the disorder of RAD51B (Extended Data Fig. 4a,b). Whereas the ATPase domains of XRCC2, RAD51D and RAD51C are all buttressed by contacts to both the ATPase domains and NTDs of neighbouring subunits, RAD51B is at the 'bottom' of the complex and there is no NTD from a preceding subunit to stabilize its ATPase domain (Fig. 1). We surmise that the intrinsically flexible nature of the RAD51B ATPase domain is due to lack of NTD stabilization. Last, although we have modelled ADP in the RAD51C ATP-binding site as it best fits the cryo-EM density, it is formally possible that it is a poorly ordered AMP-PNP molecule.

To investigate contributions of individual BCDX2 subunits to DNA-stimulated ATP hydrolysis[6], we purified RAD51B–RAD51C (BC) and RAD51D–XRCC2 (DX2) subcomplexes and found that BC, but not DX2, exhibited DNA-stimulated ATPase activity. Together with the structural information, these results indicate that the ATP hydrolytic centre of BCDX2 resides within RAD51B and/or RAD51C (Extended Data Fig. 4c). Notably, ATP hydrolysis was consistently lower on mixing BC and DX2 than for BC alone, suggesting that DX2 downregulates ATP hydrolysis by BC (Extended Data Fig. 4c). Last, we found that substitution of the RAD51C Walker A motif lysine residue 131 to alanine greatly impairs ATPase activity without affecting BDCX2 stability (Extended Data Fig. 4d). This lysine residue is also highly conserved in the Walker A motifs of other ATPases including human RAD51 (ref. 25).

BCDX2 DNA substrate specificity

We next sought to gain insights into the DNA-binding site of BCDX2 and the basis of ssDNA specificity[26]. Two flexible loops, L1 and L2, within RAD51 provide most contacts with ssDNA and double-stranded DNA (dsDNA) in presynaptic and postsynaptic complexes, respectively[19,24,27]. Analysis of the surface electrostatics of our BCDX2 structure reveals a highly basic surface formed in large part by L1 and L2 of RAD51C and RAD51D, which resembles that of RAD51 nucleofilaments[19,24,28] (Fig. 3a). This basic surface is extended on one side of the core RAD51C and RAD51D module by XRCC2 L1 and L2, and docking of the RAD51B ATPase domain onto RAD51C shows that the basic surface extends along RAD51B on the other side of BCDX2 (Fig. 3a and Extended Data Fig. 3h).

We subsequently determined a cryo-EM structure of BCDX2 bound to poly(C) ssDNA at a nominal resolution of 3.1 Å (masked; Fig. 3b–e, Extended Data Figs. 5 and 6 and Extended Data Table 1). Unambiguous density for six nucleotides was evident that spans a contiguous basic surface on the RAD51C, RAD51D and XRCC2 (CDX2) subunits of BCDX2 (Fig. 3b). Consistent with this observation, our results showed that BCDX2 binds ssDNA much more avidly than BC or DX2 (Fig. 3f,g). Moreover, whereas the BCD heterotrimer exhibits modest DNA binding activity, the DNA binding activity of the CDX2 heterotrimer is comparable to that of BCDX2 suggesting that RAD51C–RAD51D interactions underpin a ssDNA binding interface that is bolstered by XRCC2 (Fig. 3f). Like apo BCDX2, the ATPase domain of RAD51B is not visible in the BCDX2–ssDNA structure indicating that ssDNA binding fails to induce contacts between the RAD51B and RAD51C ATPase domains. There was also clear density for AMP-PNP within the ATP-binding sites of RAD51D and XRCC2 as in apo BCDX2 (Extended Data Fig. 6d). In contrast to the case for apo BCDX2, in which the active site of RAD51C harbours density consistent with ADP or poorly ordered AMP-PNP (Extended Data Fig. 2d), strong density for AMP-PNP is present in the active site of RAD51C in ssDNA-bound BCDX2 (Extended Data Fig. 6d).

Residues from RAD51D and XRCC2 contact four and three nucleotides of the ssDNA, respectively. Nearly all residues contacting the sugar phosphate backbone of the ssDNA are located within the L2 loops of RAD51C, RAD51D and XRCC2 (Fig. 3b,c,e). Backbone amide nitrogen atoms of Arg253, Leu264, Gly265 and Arg266 of RAD51D and Gln200 of XRCC2 and the side chains of Thr259 and Ser304 of RAD51C, Arg266 of RAD51D, and Arg224 of XRCC2 participate in hydrogen bonds to the ssDNA phosphate backbone (Fig. 3b). Nearly all contacts to the cytosine bases of ssDNA are mediated by L1 residue side chains of RAD51C, RAD51D and XRCC2 (Fig. 3b,e). Side chains of Ser256 of RAD51C, Arg221 and Arg253 of RAD51D, and Arg159 of XRCC2 engage in hydrogen bond-mediated contacts to the cytosine bases of the ssDNA. Accordingly, BCDX2 formed by mixing BC and DX2 with either the R266A alteration in RAD51D or the R159A alteration in XRCC2 strongly or moderately impairs DNA binding, respectively (Fig. 3g). Notably, comparable DNA binding activity was seen in BCDX2 purified as a tetramer or reconstituted by mixing wild-type (WT) BC with DX2 (Fig. 3g). Additional patchy density projects from the 3′ end of the ssDNA towards Arg249 and Arg258 of RAD51C (Fig. 3b,c). This suggests weak interactions between RAD51C and one or two additional nucleotides at the 3′ end of the ssDNA continuing along the conserved basic surface of BCDX2.

Comparison of ssDNA-bound BCDX2 and RAD51 structures shows that, although the basic patch comprising the DNA-binding site is well conserved, there are substantial differences in how ssDNA is engaged (Fig. 3c–e). This includes substantial diversity of L1 and L2 residues involved in ssDNA contacts and differences in the ssDNA paths, particularly at the 5′ end (Fig. 3b–e). Whereas RAD51 binds ssDNA in nucleotide triplets with L2 inserted into the space between triplet repeats[24], BCDX2 engages ssDNA in a less regular manner without such a role for L2 (Fig. 3b,e). Furthermore, RAD51 residues involved in ssDNA contacts are poorly conserved in BCDX2 subunits (0–23% identity; 20–36% similarity) and there are more contacts to the nitrogenous bases in the BCDX2–ssDNA structure (Fig. 3b,e). Also notable is the lack of conservation of RAD51 Arg235 in BCDX2 subunits, which is involved in dsDNA engagement and DNA strand exchange by RAD51 (Fig. 3e; PDB 7EJE; ref. 19). Last, there is variability in the length of L1, with RAD51B and XRCC2 being two residues and one residue longer than the corresponding loop in RAD51, and RAD51C and RAD51D being three and two residues shorter, respectively (Fig. 3e).

To gain insights into the basis of BCDX2 specificity for ssDNA and for the altered path of ssDNA in the BCDX2 and RAD51 structures, we superimposed the RAD51C ATPase domain onto the RAD51 subunit contacting the ssDNA 3′ end in the presynaptic RAD51–ssDNA complex (Extended Data Fig. 7a,b). The ATPase domains of RAD51C and RAD51 superimpose well (root mean square deviation ≈ 1.5 Å), but our analysis reveals substantial differences in subunit positioning for BCDX2 and RAD51 (Extended Data Fig. 7a,b). Whereas most ATPase domain contacts at the interface between RAD51C and RAD51D, RAD51D and XRCC2, and RAD51 subunits are conserved (Extended Data Figs. 4a,b and 8), the RAD51C linker and ATPase domain of RAD51D tilt as a rigid body by about 11° relative to the second RAD51 subunit in the superposition (RAD51.2; Extended Data Fig. 7a). An even greater rigid-body tilting of about 23° of the RAD51D linker and XRCC2 ATPase domain relative to the third RAD51 subunit in the superposition occurs (RAD51.3; Extended Data Fig. 7b).

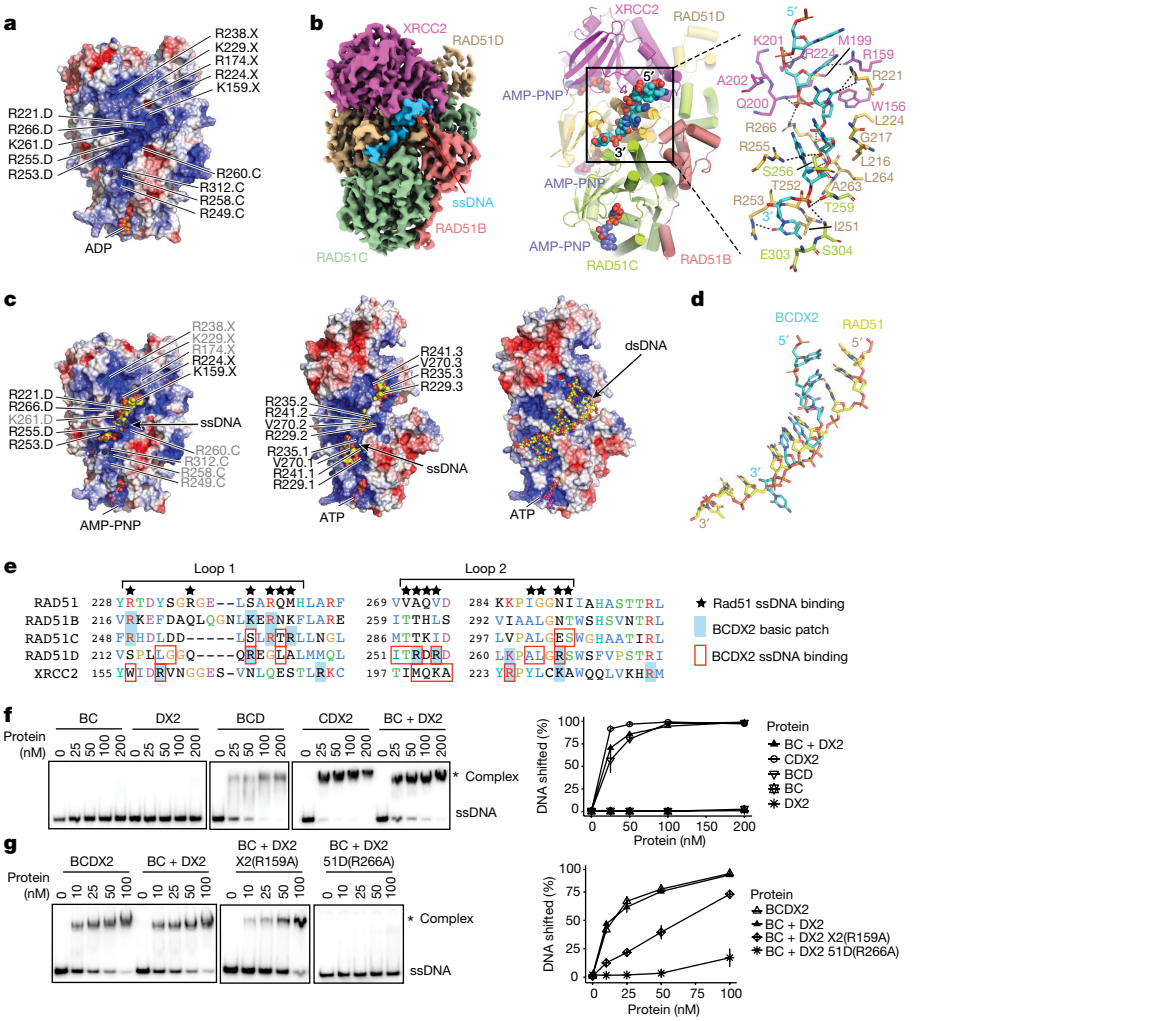


Fig. 3 | Structural and functional analysis of the ssDNA-binding site of BCDX2. a, Surface electrostatic representation of apo BCDX2 with residues comprising a highly basic surface (blue) labelled. **b**, Left, cryo-EM map of the BCDX2–ssDNA complex. Centre, schematic of the BCDX2–ssDNA complex. Right, magnified view of the BCDX2–ssDNA interface with ssDNA and ssDNA-interacting residues of BCDX2 shown as sticks. **c**, Surface electrostatic representations of BCDX2–ssDNA (left), RAD51 presynaptic (PDB 7EJC; middle) and RAD51 postsynaptic (PDB 7EJE; right) complexes with ssDNA shown as spheres. ssDNA-interacting residues are labelled with black text; residues from the BCDX2 basic patch not directly contacting ssDNA are labelled with grey text. Subunit identity for the BCDX2 complex is appended to the amino acid label (for example, R255 of RAD51D as R255.D). **d**, ssDNA from BCDX2- and RAD51-bound complexes shown as sticks in the same view as in **c**. **e**, Structure-based sequence alignment of RAD51 and BCDX2 ssDNA-binding sites. Residues are labelled as indicated in the legend on the right. **f**, Left, ssDNA binding by the BCDX2 subcomplexes at indicated concentrations assessed by electrophoretic mobility shift assays using an 80-nucleotide substrate. Right, results from three independent experiments plotted as mean values ± s.d. **g**, ssDNA binding by BCDX2 comparing WT and mutants defective in DNA binding in RAD51D or XRCC2 was analysed as in **f** at the indicated protein concentrations. X2, XRCC2; 51D, RAD51D. The gel images in **f**,**g** were derived from same experiment and processed in parallel.

Superposition of the postsynaptic RAD51–dsDNA structure[19,24] onto our BCDX2–ssDNA structure reveals steric clashes between the complementary DNA strand and L1 of XRCC2 (Extended Data Fig. 7c). These clashes stem from the tilting of BCDX2 subunits relative to RAD51 and from structural differences within and in proximity to L1 of XRCC2, including an extension and altered orientation of H12, which imparts rigidity to this region (Extended Data Fig. 7b,d). Although clashes occur with ssDNA and dsDNA in the model, the higher flexibility of ssDNA should allow it to sample different paths within the DNA-binding groove of BCDX2 (Fig. 3c,d). This is particularly evident at the ssDNA 5′ end in our structure where the backbone of the first three ordered nucleotides is flipped nearly 180° relative to the RAD51–ssDNA structure, thereby circumventing the most severe steric clashes that would occur through the RAD51–ssDNA path (Fig. 3c,d). Given that dsDNA is bulkier and less flexible, sampling of available paths would be restricted by L1 of XRCC2 and by the location of the NTDs proximal to this loop (Extended Data Fig. 7c).

HR mediator activity of BCDX2

We used single-molecule DNA curtain analysis to define the HR mediator role of BCDX2. For this, we generated BCDX2 tagged with GFP on either RAD51C or XRCC2. We could readily detect an association of BCDX2 with RPA–ssDNA in reactions containing ATP (Fig. 4a–c) but not when ATP was omitted (Extended Data Fig. 9a). Association of BCDX2 with RPA–ssDNA was transient (Fig. 4a,b), and analysis of the GFP-tagged RAD51C form of BCDX2 and ssDNA bound by mCherry–RPA yielded a dissociation rate constant (k_{off}) of 0.471 min^{-1} with a 95% confidence interval (CI) of 0.433 to 0.510 (Fig. 4c). Similar results were obtained with either GFP-tagged XRCC2 or unlabelled RPA (Fig. 4b,c). Notably, BCDX2 remained tightly bound to RPA–ssDNA when the non-hydrolysable ATP analogue ATPγS or AMP-PNP was present, indicative of ATP hydrolysis playing a regulatory role in the turnover dynamics of BCDX2 (Extended Data Fig. 9a). Note, the DNA curtain assays can be carried out with

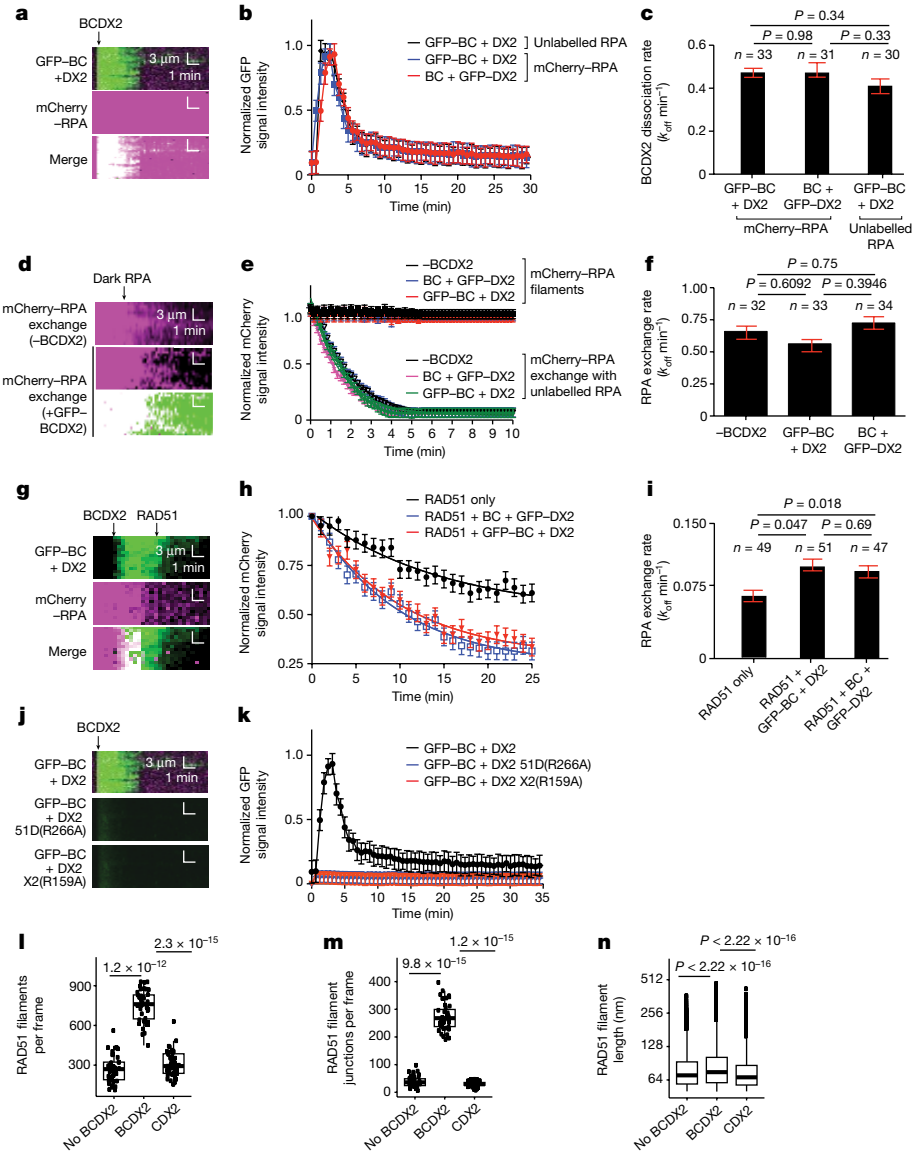


Fig. 4 | Characterization of BCDX2 recombination mediator activity. **a**, Kymographs showing GFP–BC + DX2 (10 nM each; green) binding and dissociating from mCherry–RPA–ssDNA (magenta). **b**, GFP signal intensity for GFP–BC + DX2 or BC + GFP–DX2 on RPA–ssDNA (unlabelled or mCherry-tagged); error bars represent 95% CIs; $n = 3$ flow cells per dataset. **c**, BCDX2 dissociation from RPA–ssDNA; error bars represent 95% CIs; $n = 3$ flow cells per dataset; P values were calculated by unpaired t-test (two-sided). **d**, mCherry–RPA exchange with unlabelled RPA ± BCDX2 (10 nM each; merged). **e**, mCherry–RPA signal (±mCherry–RPA exchange). Data represent mCherry signal; error bars represent 95% CIs; $n = 3$ flow cells per dataset. **f**, mCherry–RPA exchange with unlabelled RPA ± BCDX2; error bars represent 95% CIs; $n = 3$ flow cells per dataset; P values were calculated by unpaired t-test (two-sided). **g**, Kymographs showing GFP–BC + DX2 (10 nM each) binding to mCherry–RPA–ssDNA followed by injection of 500 nM RAD51. **h**, mCherry–RPA dissociation during RAD51 filament assembly ± BCDX2. Data represent mCherry signal; error bars represent 95% CIs; $n = 3$ flow cells per dataset. **i**, mCherry–RPA dissociation from ssDNA during RAD51 filament assembly; error bars represent 95% CIs; $n = 3$ flow cells per dataset; P values were calculated by unpaired t-test (two-sided). **j**, Kymographs of BCDX2 variants (10 nM each) binding to mCherry–RPA–ssDNA. **k**, Graph quantifying BCDX2 binding to mCherry–RPA–ssDNA. The kymograph and graph for GFP–BC + DX2 (+ATP) are reproduced from **a**,**b**, for comparison. Data are represented as mean GFP signal; error bars represent 95% CIs; $n = 3$ flow cells per dataset. **l**–**n**, Box plots depicting number of RAD51 nucleoprotein filaments per frame (**l**), number of junctions formed by filaments per frame (**m**) and length of filaments in nanometres (**n**) measured by negative-stain EM in absence or presence of BCDX2 and CDX2. Data depict quantification from at least 40 electron micrographs (**l**,**m**) or 11,271 filaments (**n**) for each sample captured in two independent experiments. The P values for the significance of differences in median values were calculated by the two-sided Mann–Whitney–Wilcoxon test. For box plots, each box depicts the interquartile range (IQR) containing 50% of the data, intersected by the median, and whiskers extend up to 1.5 IQR value.

RPA–ssDNA but not naked ssDNA, because RPA is essential for minimizing secondary structure to allow ssDNA to adopt an extended state in the sample chamber for visualization by total internal reflection fluorescence microscopy[29]. Even though RPA binds ssDNA with picomolar affinity, it undergoes rapid exchange with free RPA[30]. Notably, although BCDX2 binds to RPA–ssDNA, we saw no evidence that it enhances either dissociation or exchange of RPA from the ssDNA (Fig. 4d–f).

We could find no evidence for interactions of BCDX2 with preassembled RAD51 filaments, nor could we detect interactions of BCDX2 with RAD51 filaments when BCDX2 and RAD51 were co-introduced into reactions containing RPA–ssDNA (Extended Data Fig. 9b). However, when RAD51 was introduced into reactions containing BCDX2 pre-bound to RPA–ssDNA, we observed a 42% to 49% increase in the rate of mCherry–RPA dissociation (Fig. 4g–i), which serves as a reliable

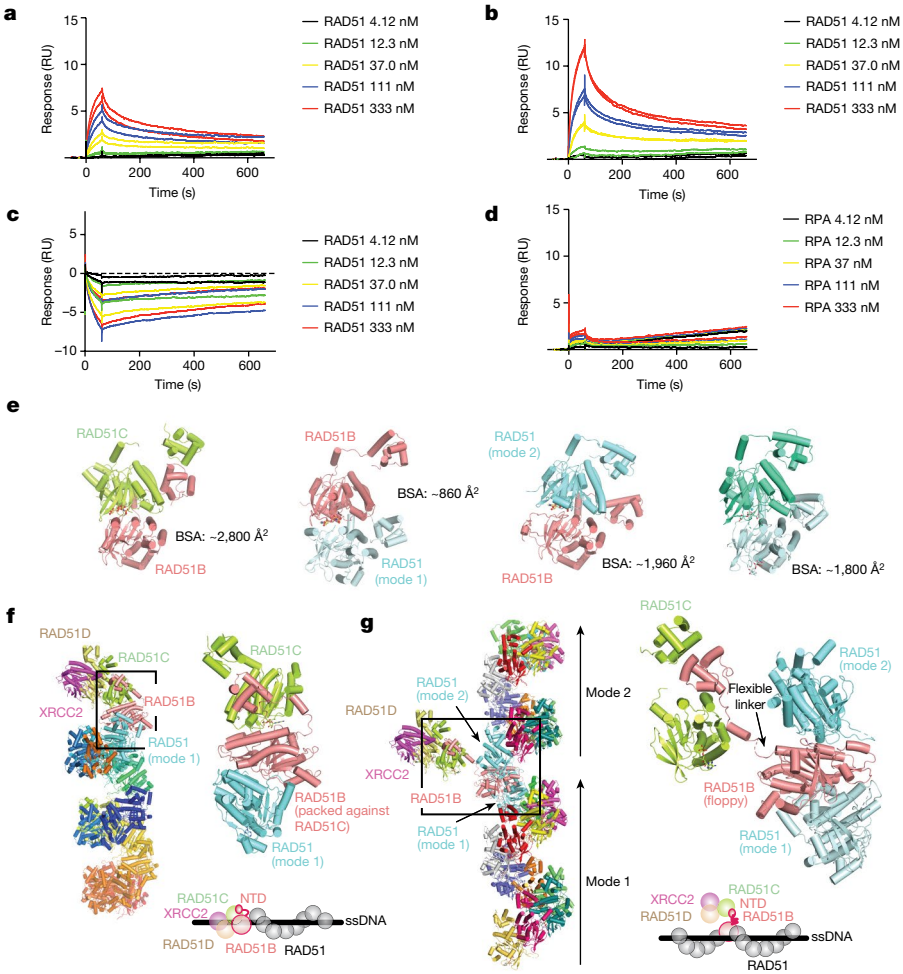


Fig. 5 | SPR analysis and AlphaFold modelling of BCDX2–RAD51 interactions. **a**–**c**, Sensorgram from SPR experiments of RAD51 binding to BCDX2 (**a**), BC (**b**) and DX2 (**c**). RU, response units. **d**, Sensorgram from SPR experiments of RPA binding to BCDX2. Two replicates of experimental responses of RAD51 or RPA binding at different concentrations are shown by colour-coded lines. **e**, AlphaFold modelling of RAD51B–RAD51C (left) and RAD51–RAD51B (middle two images). Two potential RAD51–RAD51B binding modes are presented; mode 1 in which the surface harbouring the primary ATP-binding site of RAD51B interacts with RAD51 (middle left image), and mode 2 in which the surface harbouring the secondary ATP-binding site of RAD51B interacts with RAD51 (middle right image). Right, the RAD51–RAD51 interface from the presynaptic complex (PDB 7EJC) is shown for comparison. Buried surface area (BSA, calculated using PISA) of the indicated regions is presented to the right of the model or structure. **f**, BCDX2–RAD51 model 1, in which the ATPase domain of RAD51B (secondary ATP-binding surface) packs against RAD51C, and RAD51 packs against the primary ATP-binding surface of RAD51B (mode 1). **g**, BCDX2–RAD51 model 2, in which a flexible RAD51B ATPase domain can engage RAD51 through binding modes 1 and/or 2. A schematic is shown at the bottom.

proxy for the rate of RAD51 filament assembly[31,32]. ATPγS and AMP-PNP trap BCDX2 on RPA–ssDNA (Extended Data Fig. 9a), but the addition of RAD51 to these trapped complexes causes BCDX2 dissociation and allows concomitant RAD51 filament assembly (Extended Data Fig. 9c,d). However, the rate for RAD51 filament assembly increased only by 24% or 20% with ATPγS or AMP-PNP, respectively, highlighting the need for ATP hydrolysis to achieve full stimulation of RAD51 filament assembly (Extended Data Fig. 9d).

Together, our results show that ATP binding is necessary for association of BCDX2 with RPA–ssDNA, ATP hydrolysis contributes to the release of BCDX2 from RPA–ssDNA, and BCDX2 bound to RPA–ssDNA accelerates RAD51 filament formation, but BDCX2 does not remain bound to fully assembled RAD51 filaments. Although there is clear evidence of BCDX2 association with RPA–ssDNA, we cannot distinguish between BCDX2 binding to ssDNA, RPA or both. As biochemical and cryo-EM analyses show that BCDX2 binds ssDNA, it is likely that the binding interactions observed in the DNA curtain assays reflect BCDX2 binding to ssDNA itself. To assess the relevance of the ssDNA-binding pocket as defined by our cryo-EM structure, we tested two alterations, RAD51D(R266A) and XRCC2(R159A), predicted to disrupt interactions with ssDNA. Notably, we found that BCDX2 harbouring either alteration shows no appreciable binding to RPA–ssDNA in DNA curtain assays (Fig. 4j,k).

Next, we analysed the effect of BCDX2 on RAD51 filaments formed on a 150-base oligonucleotide by negative-stain EM (Fig. 4l–n and Extended Data Fig. 10a). Notably, the number of RAD51 nucleoprotein filaments per micrograph was significantly higher in the presence of BCDX2 (Fig. 4l). However, we did not observe any substantial increase in RAD51 filament length on adding BCDX2 (Fig. 4n). A significant increase in the number of interconnected RAD51 filaments was seen with BCDX2 present (Fig. 4m). These findings suggest that BCDX2 promotes RAD51 filament formation by increasing the local concentration of RAD51 and DNA, which is also supported by a previous study showing RAD51 filaments forming in proximity of BCDX2-bound DNA[11]. We also tested the trimeric CDX2 subcomplex, which can bind ssDNA as efficiently as BCDX2 (Fig. 3f) but lacks RAD51B. Notably, CDX2 was unable to promote

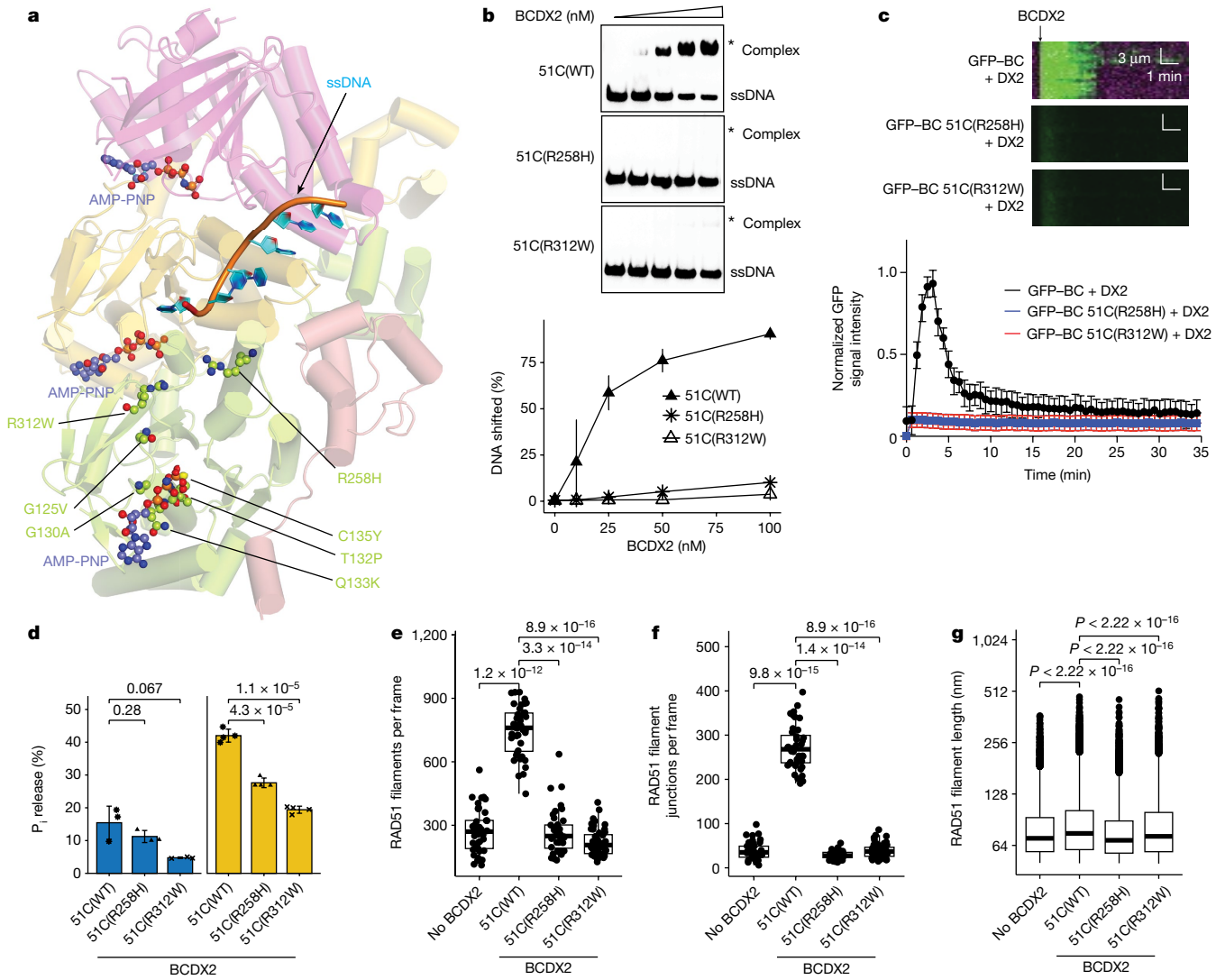


Fig. 6 | Structural and functional analysis of BCDX2 subunit alterations from patients with cancer. a, The overall BCDX2–ssDNA structure shown as a semitransparent schematic representation with amino acids of BCDX2 subunit alterations derived from patients with cancer shown as solid spheres. **b**, ssDNA binding by the WT and indicated mutant BCDX2 complexes assessed by electrophoretic mobility shift assays using an 80-nucleotide substrate (top), and measurements for three independent experiments plotted as mean values ± s.d. (bottom). The gel images were derived from the same experiment and processed in parallel. **c**, Representative kymographs of single ssDNA molecules (top) showing the indicated GFP–BCDX2 variant (10 nM each protein complex) in the presence of 2.5 mM ATP binding to and dissociating from mCherry–RPA–ssDNA. The graph (bottom) shows quantification of GFP–BCDX2 binding to mCherry–RPA–ssDNA. The kymograph and graph for GFP–BC + DX2 (+ATP) are reproduced from Fig. 4a,b, for comparison. Data are represented as mean normalized GFP signal intensity; error bars represent 95% CIs. Data were derived using three flow cells per reaction condition. **d**, Histograms depicting ATP hydrolysis with 1 µM WT and indicated mutant BCDX2 complexes with (phiX174 virion; right) or without (left) ssDNA after 60-min incubation (measurements for three independent experiments are plotted as mean values ± s.d). 51C, RAD51C. *P* values were calculated as indicated in Extended Data Fig. 4c. **e**–**g**, Box plots depicting the number of RAD51 nucleoprotein filaments per frame (**e**), number of junctions formed by filaments per frame (**f**) and length of filaments in nanometres (**g**) measured by negative-stain EM in the absence or presence of WT BCDX2 (reproduced from Fig. 4l–n, for comparison) or BCDX2 with the RAD51C mutants R258H and R312W. Data depict quantifications from at least 40 electron micrographs (**e**,**f**) or 11,271 filaments (**g**) for each sample captured in two independent experiments. The *P* value calculations and box plot descriptions are the same as in Fig. 4l–n.

RAD51 filament formation (Fig. 4l–n). The results reveal a role of RAD51B in the promotion of RAD51 filament formation by BCDX2.

Modelling a BCDX2–RAD51 complex

We surmised that the HR mediator activity of BCDX2 may entail an interaction with RAD51. Indeed, surface plasmon resonance (SPR) analysis showed that RAD51 interacts with BCDX2 and also the BC subcomplex with comparable affinities, but no interaction with the DX2 subcomplex was observed (Fig. 5a–c and Extended Data Table 2). The interaction of RAD51 with BCDX2 and the BC subcomplex was also validated by mass photometry (Extended Data Fig. 10b,c), suggesting that the RAD51 interaction interface resides within the BC module of BCDX2. Moreover, we did not observe an interaction of BCDX2 with RPA (Fig. 5d), consistent with the premise that the association of BCDX2 with RPA–ssDNA (Fig. 4a) is primarily through ssDNA binding by BCDX2.

Structural analysis and modelling were conducted to gain insights into the molecular basis of interactions between BCDX2 and RAD51. It is unlikely that RAD51 interacts with BCDX2 through XRCC2, as modelling shows that sandwiching of an ATP molecule between XRCC2 and

an adjacent RAD51 monomer would be blocked by steric impediments in XRCC2 (Extended Data Fig. 10d). By contrast, there is no structural impediment to interaction of RAD51 with BCDX2 on the RAD51B side. AlphaFold[33] analysis of RAD51B–RAD51C yields a model in which the ATPase domains pack against each other in a similar way to other subunits in the BCDX2 and RAD51 complexes (Fig. 5e). Additional AlphaFold analysis of RAD51–RAD51B yielded a model in which key structural elements of RAD51 pack against the ATP-binding site of RAD51B (mode 1; Fig. 5e,f). In the resulting RAD51–BCDX2 model, XRCC2 is situated at the 5′ end of the ssDNA-binding site, with a RAD51 nucleoprotein filament emanating from the bottom (3′ end) of BCDX2 (model 1; Fig. 5f).

We also considered mechanistic implications of the highly dynamic nature of the RAD51B ATPase domain. Accordingly, we modelled the standalone RAD51–RAD51B interaction (for example, not in the context of BCDX2), which yielded a model in which key structural elements of RAD51B are positioned in proximity to the ATP-binding site of RAD51, similar to the RAD51B–RAD51C interaction (Fig. 5e). This 'mode 2' RAD51–RAD51B model has about 1,250 Å^2 of surface area buried at the interface between the ATPase domains, which is substantially greater than the approximately 560 Å^2 buried at the RAD51–RAD51B mode 1 interface (Fig. 5e). Given its conformational flexibility, the RAD51B ATPase domain may interact with RAD51 presynaptic filaments through mode 1 and/or mode 2. RAD51–RAD51B interaction through mode 2 could impart structural plasticity to facilitate the assembly of a nascent RAD51 filament on ssDNA. This could be relevant at locations involving junctions between ssDNA and dsDNA during HR and/or could lead to recruitment of additional HR factors (Fig. 5g).

Impact of RAD51C cancer alterations

Previously, we demonstrated that patient-derived alterations in and around the Walker A ATP-binding motif of RAD51C impair DNA binding and ATP hydrolysis by BCDX2 biochemically, and they also affect cellular viability and engender hypersensitivity to DNA-damaging agents and defective HR[6] (Fig. 6a). Here we focused on patient-derived alterations in non-catalytic amino acid residues of RAD51C that cause defects in RAD51C and RAD51D interactions and HR in cell-based assays[6].

RAD51C(R258H) is the only reported alteration for Fanconi anaemia complementation group O (ref. 16), and mutation of the germline causing RAD51C(R312W) leads to a predisposition to breast and ovarian cancer[3,6,34]. Notably, RAD51C R258 is equivalent to RAD51 R241 (ref. 6), a key residue involved in DNA binding[24]. Both alterations cause severe HR defects in cell-based assays and in RAD51C–RAD51D interactions[6]. We found that these pathogenic alterations strongly impair DNA binding (Fig. 6b) and modestly impair DNA-stimulated ATP hydrolysis (Fig. 6d and Extended Data Fig. 10e) by BCDX2. Both alterations abolish BCDX2 interactions with RPA–ssDNA in DNA curtain assays (Fig. 6c) and, like WT BCDX2, BCDX2 mutants do not interact with preassembled RAD51 filaments (Extended Data Fig. 9b). Notably, both BCDX2 mutants fail to promote RAD51–ssDNA filament assembly (Fig. 6e–g and Extended Data Fig. 10a). We note that Arg258 and Arg312 of RAD51C are proximally located to cryo-EM density extending from the 3′-most modelled nucleotide in our BCDX2–ssDNA structure (Fig. 3b,c). Together, our results indicate that pathogenicity of the RAD51C(R258H) and RAD51C(R312W) alterations stems from disruption of interactions with DNA.

Our work helps to define the overall architecture of BCDX2 and yields insights into the nucleotide dependence and DNA substrate specificity profile of this complex. Our results also shed light on how DNA and ATP binding and hydrolysis relate to complex assembly and disassembly, which in turn regulate BCDX2 function. Our single-molecule analysis indicates that BCDX2 binds RPA–ssDNA in an ATP-dependent manner and that ATP hydrolysis mediates BCDX2 dissociation. We have also shown that association of BCDX2 with RPA–ssDNA substantially increases the rate of RAD51–ssDNA filament assembly. Overall, our results indicate that BCDX2 functions similarly to the *Saccharomyces cerevisiae* complex of *RAD51* paralogue products Rad55–Rad57 and the *Caenorhabditis elegans* complex of paralogue products RFS-1–RIP-1 by stimulating Rad51–ssDNA nucleoprotein filament assembly without any stable association with mature RAD51 filaments[35–37]. The key mechanistic difference distinguishing BCDX2 from Rad55–Rad57 and RFS-1–RIP-1 is that the last two complexes do not stably interact with RPA–ssDNA, but instead co-bind to RPA–ssDNA with Rad51 to promote filament assembly and then quickly dissociate from the resulting Rad51–ssDNA complexes[35,36]. By contrast, we now show that BCDX2 engages RPA–ssDNA before the arrival of RAD51 to then stimulate RAD51 filament assembly, thus revealing a new mode of action for products of *RAD51* paralogues. We note that the interaction between BCDX2 and RPA–ssDNA is mediated through contacts to ssDNA as we fail to observe direct interaction between BCDX2 and RPA (Fig. 5d). Although our SPR, mass photometry and modelling analyses indicate that BCDX2 physically interacts with RAD51, the structural basis of this interaction and its functional impact on the HR mediator activity of BCDX2 remain to be determined. Also unknown is the role of the RAD51B ATPase domain in regulating the function of the BCDX2. In sum, our work provides a substantial step forward in our understanding of the structure and function of BCDX2 and lays the groundwork for answering remaining questions regarding how it and other complexes comprising the products of *RAD51* paralogues act as mediators of RAD51 presynaptic filament assembly during HR.

Online content

Any methods, additional references, Nature Portfolio reporting summaries, source data, extended data, supplementary information, acknowledgements, peer review information; details of author contributions and competing interests; and statements of data and code availability are available at https://doi.org/10.1038/s41586-023-06219-w.

1. Sung, P. & Klein, H. Mechanism of homologous recombination: mediators and helicases take on regulatory functions. *Nat. Rev. Mol. Cell Biol.* **7**, 739–750 (2006).
2. Sullivan, M. R. & Bernstein, K. A. RAD-ical new insights into RAD51 regulation. *Genes* https://doi.org/10.3390/genes9120629 (2018).
3. Meindl, A. et al. Germline mutations in breast and ovarian cancer pedigrees establish *RAD51C* as a human cancer susceptibility gene. *Nat. Genet.* **42**, 410–414 (2010).
4. Kondrashova, O. et al. Secondary somatic mutations restoring RAD51C and RAD51D associated with acquired resistance to the PARP inhibitor rucaparib in high-grade ovarian carcinoma. *Cancer Discov.* **7**, 984–998 (2017).
5. Garcin, E. B. et al. Differential requirements for the RAD51 paralogs in genome repair and maintenance in human cells. *PLoS Genet.* **15**, e1008355 (2019).
6. Prakash, R. et al. Homologous recombination-deficient mutation cluster in tumor suppressor. *Proc. Natl Acad. Sci. USA* **119**, e2202727119 (2022).
7. Clarke, T. L. & Mostoslavsky, R. DNA repair as a shared hallmark in cancer and ageing. *Mol. Oncol.* **16**, 3352–3379 (2022).
8. Prakash, R., Zhang, Y., Feng, W. & Jasin, M. Homologous recombination and human health: the roles of BRCA1, BRCA2, and associated proteins. *Cold Spring Harb. Perspect. Biol.* **7**, a016600 (2015).
9. Sigurdsson, S., Trujillo, K., Song, B., Stratton, S. & Sung, P. Basis for avid homologous DNA strand exchange by human Rad51 and RPA. *J. Biol. Chem.* **276**, 8798–8806 (2001).
10. Zhao, W. et al. Promotion of BRCA2-dependent homologous recombination by DSS1 via RPA targeting and DNA mimicry. *Mol. Cell* **59**, 176–187 (2015).
11. Masson, J. Y. et al. Identification and purification of two distinct complexes containing the five RAD51 paralogs. *Genes Dev.* **15**, 3296–3307 (2001).
12. Martino, J. et al. The human Shu complex functions with PDS5B and SPIDR to promote homologous recombination. *Nucleic Acids Res.* **47**, 10151–10165 (2019).
13. Yonetani, Y. et al. Differential and collaborative actions of Rad51 paralog proteins in cellular response to DNA damage. *Nucleic Acids Res.* **33**, 4544–4552 (2005).
14. Nalepa, G. & Clapp, D. W. Fanconi anaemia and cancer: an intricate relationship. *Nat. Rev. Cancer* **18**, 168–185 (2018).
15. Jacquinet, A. et al. Expanding the FANCO/RAD51C associated phenotype: cleft lip and palate and lobar holoprosencephaly, two rare findings in Fanconi anemia. *Eur. J. Med. Genet.* **61**, 257–261 (2018).
16. Vaz, F. et al. Mutation of the *RAD51C* gene in a Fanconi anemia-like disorder. *Nat. Genet.* **42**, 406–409 (2010).
17. Shamseldin, H. E., Elfaki, M. & Alkuraya, F. S. Exome sequencing reveals a novel Fanconi group defined by XRCC2 mutation. *J. Med. Genet.* **49**, 184–186 (2012).
18. Miller, K. A., Sawicka, D., Barsky, D. & Albala, J. S. Domain mapping of the Rad51 paralog protein complexes. *Nucleic Acids Res.* **32**, 169–178 (2004).
19. Xu, J. et al. Mechanisms of distinctive mismatch tolerance between Rad51 and Dmc1 in homologous recombination. *Nucleic Acids Res.* **49**, 13135–13149 (2021).

20. Pellegrini, L. et al. Insights into DNA recombination from the structure of a RAD51-BRCA2 complex. *Nature* **420**, 287–293 (2002).
21. Rajendra, E. & Venkitaraman, A. R. Two modules in the BRC repeats of BRCA2 mediate structural and functional interactions with the RAD51 recombinase. *Nucleic Acids Res.* **38**, 82–96 (2010).
22. Yu, D. S. et al. Dynamic control of Rad51 recombinase by self-association and interaction with BRCA2. *Mol. Cell* **12**, 1029–1041 (2003).
23. Short, J. M. et al. High-resolution structure of the presynaptic RAD51 filament on single-stranded DNA by electron cryo-microscopy. *Nucleic Acids Res.* **44**, 9017–9030 (2016).
24. Xu, J. et al. Cryo-EM structures of human RAD51 recombinase filaments during catalysis of DNA-strand exchange. *Nat. Struct. Mol. Biol.* **24**, 40–46 (2017).
25. Chi, P., Van Komen, S., Sehorn, M. G., Sigurdsson, S. & Sung, P. Roles of ATP binding and ATP hydrolysis in human Rad51 recombinase function. *DNA Repair* **5**, 381–391 (2006).
26. Sullivan, M. R. et al. Long-term survival of an ovarian cancer patient harboring a RAD51C missense mutation. *Cold Spring Harb. Mol. Case Stud.* https://doi.org/10.1101/mcs.a006083 (2021).
27. Matsuo, Y., Sakane, I., Takizawa, Y., Takahashi, M. & Kurumizaka, H. Roles of the human Rad51 L1 and L2 loops in DNA binding. *FEBS J.* **273**, 3148–3159 (2006).
28. Yang, H., Zhou, C., Dhar, A. & Pavletich, N. P. Mechanism of strand exchange from RecA-DNA synaptic and D-loop structures. *Nature* **586**, 801–806 (2020).
29. Gibb, B., Silverstein, T. D., Finkelstein, I. J. & Greene, E. C. Single-stranded DNA curtains for real-time single-molecule visualization of protein-nucleic acid interactions. *Anal. Chem.* **84**, 7607–7612 (2012).
30. Gibb, B. et al. Concentration-dependent exchange of replication protein A on single-stranded DNA revealed by single-molecule imaging. *PLoS ONE* **9**, e87922 (2014).
31. Ma, C. J., Gibb, B., Kwon, Y., Sung, P. & Greene, E. C. Protein dynamics of human RPA and RAD51 on ssDNA during assembly and disassembly of the RAD51 filament. *Nucleic Acids Res.* **45**, 749–761 (2017).
32. Ma, C. J., Steinfeld, J. B. & Greene, E. C. Single-stranded DNA curtains for studying homologous recombination. *Methods Enzymol.* **582**, 193–219 (2017).
33. Jumper, J. et al. Highly accurate protein structure prediction with AlphaFold. *Nature* **596**, 583–589 (2021).
34. Gayarre, J. et al. Characterisation of the novel deleterious RAD51C p.Arg312Trp variant and prioritisation criteria for functional analysis of RAD51C missense changes. *Br. J. Cancer* **117**, 1048–1062 (2017).
35. Belan, O. et al. Single-molecule analysis reveals cooperative stimulation of Rad51 filament nucleation and growth by mediator proteins. *Mol Cell* **81**, 1058–1073 (2021).
36. Roy, U. et al. The Rad51 paralog complex Rad55-Rad57 acts as a molecular chaperone during homologous recombination. *Mol. Cell* **81**, 1043–1057 (2021).
37. Špírek, M., Taylor, M. R. G., Belan, O., Boulton, S. J. & Krejci, L. Nucleotide proofreading functions by nematode RAD51 paralogs facilitate optimal RAD51 filament function. *Nat. Commun.* **12**, 5545 (2021).

Publisher's note Springer Nature remains neutral with regard to jurisdictional claims in published maps and institutional affiliations.

Springer Nature or its licensor (e.g. a society or other partner) holds exclusive rights to this article under a publishing agreement with the author(s) or other rightsholder(s); author self-archiving of the accepted manuscript version of this article is solely governed by the terms of such publishing agreement and applicable law.

© The Author(s), under exclusive licence to Springer Nature Limited 2023

Methods

Protein expression and purification

BCDX2 purification was carried as previously described[6]. In brief, BCDX2 (RAD51B–His and XRCC2–Flag) was expressed in Hi5 insect cells using baculoviruses and all of the purification steps were carried out at 0–4 °C. All baculoviruses were produced in SF9 insect cells using standard procedures. SF9 and Hi5 cells were purchased from Expression Systems and Invitrogen, respectively, and were not further authenticated. SF9 and Hi5 cells were not tested for mycoplasma contamination as they were used only for baculovirus generation and recombinant protein expression. The cell pellet was resuspended in T buffer (25 mM Tris-HCl, pH 7.5, 10% glycerol, 0.5 mM EDTA, 1 mM dithiothreitol (DTT), 0.05% IGEPAL CA-630 (Sigma), 1 mM phenylmethylsulfonyl fluoride and protease inhibitors) containing 300 mM KCl (T300), 5 mM ATP and 2 mM $MgCl_2$ and lysed by sonication, clarified lysate was incubated with Ni-NTA resin, and BCDX2 protein was eluted with T buffer containing 100 mM KCl (T100) with 200 mM imidazole. For further purification, protein was fractionated on a HiTrap Q HP column with 150–600 mM KCl gradient, and concentrated pooled fractions were subjected to size-exclusion chromatography in a Superdex200 Increase 10/300 GL column in T300 buffer with 2 mM each of ATP and $MgCl_2$. BCDX2 sample preparation for cryo-EM was otherwise carried out similarly except that size-exclusion chromatography was carried out in HEPES buffer without glycerol and IGEPAL CA-630 and with 50 mM KCl, 0.2 mM ATP and 1 mM $MgCl_2$. Peak fractions were concentrated and incubated with otherwise similar HEPES buffer but ATP replaced with 1 mM AMP-PNP for 3 h and AMP-PNP was further enriched by buffer exchange during concentration.

For BC (RAD51B–His and RAD51C or GFP–RAD51C), BCD (RAD51B–His, RAD51C and RAD51D), DX2 (RAD51D and XRCC2–Flag or GFP–XRCC2–Flag) and CDX2 (RAD51C, RAD51D and XRCC2–Flag) purification, crude cell lysates were prepared from 6–8 g cell pellet (from 800 ml insect cell culture) by sonication in 50 ml T300 with 5 mM ATP, and 2 mM $MgCl_2$, followed by centrifugation at 100,000*g* for 60 min. For BC and BCD purification, clarified lysate was incubated with 2.5 ml Ni-NTA resin (Qiagen, 1018142) for 1 h, followed by sequential washes of the resin with 25 ml T300 buffer, 500 ml T buffer with 1,000 mM KCl (T1000) and 25 ml T100 buffer and with all of the buffers also containing 20 mM imidazole, and 2 mM each of ATP and $MgCl_2$. The BC and BCD complexes were eluted from the affinity matrix with 10 ml T100 buffer containing 200 mM imidazole and 2 mM each of ATP and $MgCl_2$. For DX2 and CDX2 purification, clarified lysates were incubated with 1 ml anti-Flag M2 resin (Sigma, A2220) for 2 h, followed by sequential washes of the resin with 100 ml T300 buffer and 50 ml T100 buffer and with all of the buffers also containing 2 mM each of ATP and $MgCl_2$. The DX2 and CDX2 complexes were eluted from the affinity matrix with 10 ml T100 buffer containing 200 ng μl^{-1} Flag peptide (Sigma, F3290) and 2 mM each of ATP and $MgCl_2$. Further purification of each subcomplex was carried out by ion exchange in a 1-ml HiTrap Q HP column fractionated with a 45-ml 150–600 mM KCl gradient in T buffer containing 2 mM each of ATP and $MgCl_2$. Peak fractions were pooled and concentrated to 0.4 ml in an Amicon 30 concentrator and then subjected to size-exclusion chromatography in a Superdex200 Increase 10/300 GL column in T300 buffer with 2 mM each of ATP and $MgCl_2$.

ULP1–6×His, 6×His–SUMO–RAD51 and untagged RPA complex were all overexpressed in *Escherichia coli* BL21 (DE3) Rosetta2 by induction with 0.5 mM IPTG at an optical density of 0.5–0.6 at 600 nm overnight at 16 °C. The crude cell lysates for ULP1–6×His and 6×His–SUMO–RAD51 were prepared from 20–25 g cell pellets (from 12-l culture) by sonication in 100 ml T buffer containing 500 mM KCl (T500), followed by centrifugation at 100,000*g* for 60 min. Each clarified lysate was incubated with 5 ml Ni-NTA resin (Qiagen, 1018142) for 1 h, followed by sequential washes of the resin with 25 ml T500 buffer, 250 ml T1000 buffer and 25 ml T100 buffer and with all of the buffers also containing 20 mM imidazole. The ULP1–6×His was eluted from the affinity matrix with 10 ml T100 buffer containing 200 mM imidazole, dialysed overnight and concentrated. 6×His–SUMO–RAD51-bound Ni-NTA resin was resuspended in 5 ml T100 buffer, and 6×His–SUMO tag was cleaved by incubating overnight with ULP1 on a rotary shaker. RAD51 protein was eluted by collecting flowthrough and sequentially washing Ni-NTA resin in T100 buffer. For further purification, RAD51 protein was fractionated with a 45-ml 150–450 mM KCl gradient in T buffer first by ion exchange in a 1-ml HiTrap Q HP column followed by a 1-ml HiTrap heparin column with a 45-ml 150–450 mM KCl gradient in T buffer, and peak fractions were concentrated and saved.

The crude cell lysate for RPA purification was prepared from 30–35 g cell pellet (from 12-l culture) by sonication in 150 ml T100 buffer, clarified lysate was fractionated through a 25-ml Affi Gel Blue column with a sodium thiocyanate gradient (500–2,000 mM, 5 column volumes) in T100 buffer, peak fractions were further fractionated through a 10-ml MacroHAP hydroxyapatite column with a phosphate gradient (10–180 mM, 6 column volumes) in T100 buffer, followed by fractionation with a 45-ml 150–450 mM KCl gradient in T buffer by ion exchange in a 1-ml HiTrap Q HP column and a 1-ml HiTrap heparin column, respectively, and peak fractions were concentrated and saved.

All protein samples were snap frozen in liquid nitrogen and stored at −80 °C.

Cryo-EM sample preparation and data acquisition

Freshly eluted apo BCDX2 complex from a gel-filtration column (Superdex200 Increase 10/300 GL) was buffer exchanged to replace ATP with AMP-PNP and concentrated to about 6 μM. The sample was immediately applied onto cryo-EM Au grids (UltrAuFoil 1.2/1.3 300 mesh, Electron Microscopy Sciences) that had been glow discharged at 20 mA for 30 s in a Quorum EMS glow discharge machine. For the BCDX2–ssDNA complex, about 6 μM apo BCDX2 was mixed with a 10-fold molar excess of a 30-base poly deoxycytidine oligonucleotide (5′-CCCCCCCCCCCCCCCCCCCCCCCCCCCCCC-3′) in the presence of 2 mM AMP-PNP. The mixture was incubated for 5 min at room temperature and then applied onto cryo-EM Au grids as for apo BCDX2. Grids were vitrified using a Vitrobot Mark IV (Thermo Fisher Scientific). Specifically, 3 μl of BCDX2 specimen was pipetted onto the grid maintained at 4 °C and 100% humidity in the Vitrobot chamber. Grids were subsequently blotted for 3 s, with a blotting force of −10 and plunged into liquid ethane. Grids were transferred into liquid nitrogen and stored at cryogenic temperatures before clipping, screening and data collection.

Data collection was carried out at 200 kV on a Glacios cryo-transmission electron microscope equipped with a Falcon IV camera and Selectris energy filter (slit width: 10 eV) at the University of Texas Health San Antonio Cryo-EM Facility. Imaging was acquired using Thermo Fisher Scientific's EPU software with an AFIS model. For apo BCDX2, a total of 1,741 image frames with EER file format were recorded with an exposure time of 7 s, a total dose of 51 $e^- Å^{-2}$ with a 5.65 $e^- px^{-1} s^{-1}$ dose rate; for the BCDX2–ssDNA complex, a total of 2,163 image frames with EER file format were recorded with an exposure time of 8.9 s, a total dose of 52 $e^- Å^{-2}$ with a 4.47 $e^- px^{-1} s^{-1}$ dose rate. A total of 6,000 micrographs for BCDX2 and 7,000 micrographs for BCDX2–ssDNA were collected with a pixel size of 0.87 Å, a nominal magnification of ×130,000, and a defocus range from −0.8 to −2.0 μm.

Cryo-EM data processing for apo and ssDNA-bound BCDX2

After data collection, images were gain corrected, dose weighted and patch motion corrected using CryoSPARC v3.3.1 (ref. 38). The exact defocus value and contrast transfer function (CTF) of each micrograph were estimated using CryoSPARC's patch CTF estimation tool. For apo BCDX2 data processing, micrograph curation with a CTF cutoff value of 5 Å resolution was applied to the data, and 5,600 micrographs were kept for particle picking. The blob picker function in CryoSPARC was used for picking and yielded around 8,000,000 particles of 100 Å diameter.

The particles were subsequently extracted at a 256-px box size without downsampling. After three rounds of light two-dimensional (2D) classification to filter noise and dissociated particles, 7,219,082 particles entered the next stages of 3D initial model reconstruction and 3D classification. Six ab initio models were generated in CryoSPARC and were further used as initial references for heterogeneous refinement. For each cycle of heterogeneous refinement, the particles from the best class were kept for the next round of heterogeneous refinement. In total, four rounds of heterogeneous refinement were carried out in CryoSPARC, with the best class from the final heterogeneous refinement containing 1,192,629 particles. This class was refined to 3.0 Å with homogeneous refinement. A final step of stringent heterogeneous refinement was further applied using the 3.0-Å map as an initial model, which segregated one class with improved resolution of 2.3 Å (based on the FSC-0.143 criterion) using masked homogeneous refinement. The final map, using a negative B-factor of −150 estimated in CryoSPARC, was used for model building.

The BCDX2–ssDNA data processing workflow was similar to that described above for apo BCDX2. Micrographs were curated with a CTF cutoff value of 5 Å resolution applied, and around 4,000 micrographs were kept for particle picking. A set of around 4,000,000 particles with 256-px-box size were fed into 2D classification and 3,406,052 particles were selected. These were used for 3D initial model generation with six classes and used four rounds of 3D heterogeneous refinement processing with six initial models as references. The final 3D heterogeneous refinement step retained 480,986 particles. This was followed by a further heterogeneous refinement with only three classes with one final class of 165,968 particles applied for homogeneous refinement, yielding a resolution of 3.12 Å. This was further refined using non-uniform refinement yielding a final resolution of 3.11 Å.

Model building and refinement

Models of RAD51B, RAD51C, RAD51D and XRCC2 were first predicted using Alphafold2 (ref. 33). After deleting the low-confidence and disordered regions of each model, RAD51B, RAD51C, RAD51D and XRCC2 were rigid-body docked into the cryo-EM map using UCSF ChimeraX[39]. All of the predicted models were fitted with high confidence except the RAD51B ATP-binding domain, which showed no density in our map. Fitting correlation values were 0.59 for RAD51C, 0.62 for Rad51D, and 0.65 for XRCC2. Further building and structural refinements were carried out using COOT version 0.9.3 (ref. 40), and further refinements of stereochemistry and secondary structure were carried out in PHENIX version V1.19.1-4122-000 using phenix.real_space_refine (ref. 41). For BCDX2–ssDNA model building, the model from the apo BCDX2 complex was directly fitted into the cryo-EM map in ChimeraX, with a fitting correlation of 0.41. COOT was used for manually building the ssDNA molecule, and PHENIX real-space refinement was used to refine the full BCDX2–ssDNA model. Both apo BCDX2 and BCDX2–ssDNA structural models were validated using wwPDB (https://validate-rcsb-2.wwpdb.org/). Figures for the cryo-EM map and models were prepared with ChimeraX version 1.4 (ref. 39) and PyMOL version 2.0 (ref. 42).

DNA binding and ATPase assays

For DNA binding, 1 nM of 5′ ^{32}P-labelled 80-nucleotide ssDNA[43] was incubated with the indicated concentration of purified BCDX2 complex in 10 µl reaction buffer (50 mM Tris-HCl, pH 7.5, 155 mM KCl, 1 mM DTT, 1 mM ATP, 1 mM $MgCl_2$ and 100 ng µl^{-1} BSA) for 10 min at 37 °C. Nucleoprotein complexes were resolved on 5% polyacrylamide gels in Tris-borate buffer (45 mM each). Gels were dried and subjected to phosphorimaging analysis with Amersham Typhoon phosphorimager (Cytiva) and the ImageQuant software (Cytiva) v8.20.

BCDX2 complexes or its subcomplexes (1 µM) were incubated in the absence or presence of ssDNA (20 µM nucleotides, phiX174 virion) in 10 µl of reaction buffer (20 mM HEPES, pH 7.5, 1 mM DTT, 1 mM $MgCl_2$ and 30 mM KCl) containing 0.05 mM ATP with 0.25 µCi [γ-^{32}P]ATP at 37 °C. Aliquots of 2 µl were withdrawn at the indicated times and mixed with 2 µl of 0.5 M EDTA to stop the reaction. The level of ATP hydrolysis was determined by layer chromatography on PEI cellulose F sheets (Millipore, 105579) in 0.375 M potassium phosphate (pH 3.5), followed by phosphorimaging analysis. Data were plotted using the R (3.6.1) package ggpubr.

Negative staining and EM

For presynaptic filament assembly, RAD51 (2 µM) was incubated with 150-base oligonucleotide (6 µM nucleotides) with or without 25 nM BCDX2 variants in reaction buffer (25 mM HEPES pH 7.5, 25 mM KCl, 1 mM $MgCl_2$ and 2 mM ATP) at 37 °C for 15 min. A droplet of 20 µl of a reaction mixture was loaded onto a glow-discharged carbon-coated 300 mesh copper grid (EMS CF300 Cu) for 1 min. After blotting with filter paper, the grid was immersed in a 20-µl droplet of the staining solution (2% uranyl acetate). The stain was removed from the grid by blotting with filter paper, and the grid was washed twice with water for 1 min. Following excess stain removal, grids were dried in air for about 3 min. Negatively stained samples of human RAD51 presynaptic filaments were examined by transmission electron microscopy. Images were processed in the Fiji ImageJ image analysis package (v2.90/1.53t), and filaments were quantified using ImageJ plugin Ridge detection. Data were plotted using the R (3.6.1) package ggpubr.

Mass photometry

Mass photometry analysis was carried out using a Refeyn TwoMP instrument. Contrast-to-mass calibration was achieved by a standard curve covering a mass range from 66 up to 480 kDa. The experiments were carried out on sample carrier slides partitioned by six-well silicone cassettes. BCDX2 purified in the absence or presence of 2 mM ATP and $MgCl_2$ each was diluted in 1× PBS buffer (137 mM NaCl, 2.7 mM KCl, 8 mM Na_2HPO_4 and 2 mM KH_2PO_4) to a final concentration of 10 nM. For analysing RAD51 interactions with BCDX2 or BC complexes, proteins were mixed in the presence of 2 mM ATP and $MgCl_2$ each and were diluted in 1× PBS buffer to a final concentration of 5 nM each. Using AcquireMP software, a blank acquisition field was first adjusted in native settings and then single particles were detected in a video recorded for 1 min at a rate of 100 frames per second in ratiometric acquisition settings. All mass photometry data were analysed with DiscoverMP software to produce mass values for each detected particle and plotted as normalized counts.

SPR

SPR experiments were carried out using a Biacore T100 (with T200 sensitivity enhanced) equipped with a CM5 sensor chip. The ligand BCDX2 (148 kDa, >90% pure on the basis of SDS–polyacrylamide gel electrophoresis) was assayed for optimal pH and then immobilized using amine-coupling chemistry. The surfaces of flow cells were activated for 7 min with a 1:1 mixture of 0.1 M *N*-hydroxysuccinimide and 0.4 M 3-(*N*,*N*-dimethylamino)propyl-*N*-ethylcarbodiimide at a flow rate of 5 µl min^{-1}. The ligand (BCDX2, BC or DX2) at a concentration of 50 µg ml^{-1} in 10 mM sodium acetate, pH 5.0, was immobilized at a density of around 200 RU, and one flow cell was left blank to serve as a reference surface. All surfaces were blocked with a 7-min injection of 1 M ethanolamine, pH 8.0. To collect kinetic binding data, the analyte RAD51 or RPA in 10 mM HEPES, pH 7.4, 150 mM NaCl, 1 mM ATP, 1 mM DTT, 1 mM $MgCl_2$, 0.05% Surfactant P20, pH 7.4, was injected over all flow cells at various concentrations as shown in Fig. 5a–d at a flow rate of 30 µl min^{-1} and at a temperature of 25 °C. The complex was allowed to associate and dissociate for 60 and 600 s, respectively. Duplicate injections (in increasing concentration order) of each sample and a buffer blank were flowed over the two surfaces. Data were collected at a rate of 10 Hz. The data were fitted to a heterogeneous ligand interaction model using the global data analysis option available within Biacore T200 evaluation software (v3.2.1).

Single-molecule DNA curtain assays

All single-molecule measurements were carried out at 37 °C. Experiments were conducted with a custom-built prism-based total internal reflection fluorescence microscope (Nikon) equipped with a 488-nm laser (Coherent Sapphire, 200 mW) and a 561-nm laser (Coherent Sapphire, 200 mW)[44]. Flow cells were assembled and ssDNA curtains were prepared as previously described[45,46]. Single-molecule data were collected using NIS-elements v5.11 (Nikon). ssDNA was generated using a 5′-biotinylated primer annealed to M13 circular ssDNA as a template, by rolling circle replication with phi29 DNA polymerase[32]. The flow cell was attached to the microfluidic system and passivated with streptavidin-containing lipid bilayer as described previously[31,44]. ssDNA was injected into the flow cell, attached to the lipid bilayer through biotin–streptavidin linkage, and aligned at the barriers by application of a constant buffer flow, and secondary structures were disrupted by flushing 500 µl of 7 M urea in BSA buffer (40 mM Tris-Cl (pH 8.0), 2 mM $MgCl_2$, 1 mM DTT and 0.3 mg ml^{-1} BSA) at a flow rate of 0.8 ml min^{-1}. Free ssDNA ends were anchored to the exposed pedestals through non-specific adsorption, as described previously[44].

BCDX2 binding to RPA filaments

Experiments were started by flushing the ssDNA curtains with BSA buffer (40 mM Tris-Cl (pH 8.0), 2 mM $MgCl_2$, 1 mM DTT and 0.3 mg ml^{-1} BSA) supplemented with 100 pM mCherry–RPA for 10 min at a flow rate of 0.8 ml min^{-1}. Then 10 nM BCDX2 (either GFP–BC plus DX2 or BC plus DX2–GFP, as indicated) was injected into the flow cells through a 150-µl injection loop in HR buffer (30 mM Tris-Ac (pH 7.5), 100 mM KCl, 1 mM $MgCl_2$, 5 mM $CaCl_2$, 2.5 mM ATP (or 2.5 mM ATPγS, as indicated), 1 mM DTT, 0.2 mg ml−1 BSA at a flow rate of 0.15 ml min^{-1}. Data were collected continuously throughout the entire process at a rate of 1 frame per 10 s.

RAD51 filament assembly in the presence of BCDX2

RAD51 filament assembly was initiated by first binding BCDX2 to pre-assembled mCherry–RPA-bound ssDNA curtains, as described above, followed by immediate injection of 500 nM RAD51 in HR buffer (30 mM Tris-Ac (pH 7.5), 100 mM KCl, 1 mM $MgCl_2$, 5 mM $CaCl_2$, 2.5 mM ATP (or 2.5 mM ATPγS or AMP-PNP, as indicated)), 1 mM DTT, 0.2 mg ml^{-1} BSA at a flow rate of 0.15 ml min^{-1}. Data were collected continuously throughout the entire process at a rate of 1 frame per 3 s. Co-injection measurements were carried under the same conditions in which 10 nM BCDX2 was premixed with the 500 nM RAD51 before injection into the flow cell.

RPA exchange in the presence of BCDX2

Experiments were started by connecting the flow cells with two syringes, separated by a valve, containing either 100 pM mCherry–RPA or 100 pM unlabelled RPA in BSA buffer (40 mM Tris-Cl (pH 8.0), 2 mM $MgCl_2$, 1 mM DTT and 0.3 mg ml^{-1} BSA) supplemented with 10 nM BCDX2 (either GFP–BC plus DX2 or BC plus DX2–GFP, as indicated). Initially, the ssDNA curtains were flushed with the mCherry–RPA- and BCDX2-containing buffer for 5 min at a flow rate of 0.8 ml min^{-1}. Then the valve was switched to the unlabelled-RPA- and BCDX2-containing buffer. Data were collected continuously throughout the entire process at a rate of 1 frame per 10 s.

Single-molecule data collection and analysis

For all two-colour images, a custom-built shuttering system was used to avoid signal bleed-through during image acquisition[44]. Images from the green (GFP) and the red (mCherry) channels are recorded independently, generating an offset by 100 ms between the excitation of each colour. This system prevents any possible signal bleed-through between the two channels. The lasers were shuttered between each acquired image to minimize photobleaching. Images were captured at an acquisition rate of 1 frame per 10 s for BCDX2 binding to RPA–ssDNA, or 1 frame per 3 s for RAD51 filament assembly in the presence of BCDX2 with a 100 ms integration time. Raw TIFF images were imported as image stacks into ImageJ, and kymographs were generated from the image stacks by defining a 1-px-wide region of interest along the long axis of the individual ssDNA molecules. All data analysis was carried out using the resulting kymographs.

To calculate BCDX2 binding kinetics to RPA–ssDNA, kymographs were generated by defining a 1-px-wide region of interest along the length of individual ssDNA filaments. Integrated signal intensity for each time point was obtained from individual kymographs and normalized using the maximum value for that kymograph. The mean and 95% CI of normalized intensities across all ssDNA molecules was plotted in GraphPad Prism (v8.4.3) for each time point using an *X*–*Y* connecting line curve. Experiments containing ATPγS or AMP-PNP were carried out using the same procedures.

To calculate assembly kinetics, kymographs were generated by defining a 1-px-wide region of interest along the length of individual ssDNA filaments. Integrated signal intensity for each time point was obtained from individual kymographs and normalized using the maximum value for that kymograph. The mean and 95% CI of normalized intensities across all ssDNA molecules was plotted for each time point, and the distribution was fitted to a single exponential decay curve using GraphPad Prism (version 8.4.3) to obtain the rate constants. Experiments containing ATPγS were carried out using the same procedures.

Reporting summary

Further information on research design is available in the Nature Portfolio Reporting Summary linked to this article.

Data availability

Atomic coordinates for apo BCDX2 and BCDX2–ssDNA complexes are available at the Research Collaboratory for Structural Bioinformatics PDB with accession codes 8FAZ and 8GBJ, respectively. The corresponding cryo-EM maps have been deposited into the Electron Microscopy Data Bank with accession numbers EMD-28961 (apo BCDX2) and EMD-29917 (BCDX2–ssDNA). The structure data used from the Research Collaboratory for Structural Bioinformatics are available at PDB 7EJC and PDB 7EJE. Source data are provided with this paper.

38. Punjani, A., Rubinstein, J. L., Fleet, D. J. & Brubaker, M. A. CryoSPARC: algorithms for rapid unsupervised cryo-EM structure determination. *Nat. Methods* **14**, 290–296 (2017).
39. Pettersen, E. F. et al. UCSF ChimeraX: structure visualization for researchers, educators, and developers. *Protein Sci.* **30**, 70–82 (2021).
40. Emsley, P. & Cowtan, K. Coot: model-building tools for molecular graphics. *Acta Crystallogr. D* **60**, 2126–2132 (2004).
41. Liebschner, D. et al. Macromolecular structure determination using X-rays, neutrons and electrons: recent developments in Phenix. *Acta Crystallogr. D* **75**, 861–877 (2019).
42. Delano, W. The PyMOL molecular graphics system http://www.pymol.org (DeLano Scientific, 2002).
43. Gaines, W. A. et al. Promotion of presynaptic filament assembly by the ensemble of *S. cerevisiae* Rad51 paralogues with Rad52. *Nat. Commun.* **6**, 7834 (2015).
44. De Tullio, L., Kaniecki, K. & Greene, E. C. Single-stranded DNA curtains for studying the Srs2 helicase using total internal reflection fluorescence microscopy. *Methods Enzymol.* **600**, 407–437 (2018).
45. Greene, E. C., Wind, S., Fazio, T., Gorman, J. & Visnapuu, M. L. DNA curtains for high-throughput single-molecule optical imaging. *Methods Enzymol.* **472**, 293–315 (2010).
46. Roy, U. & Greene, E. C. Single-stranded DNA curtains for single-molecule visualization of Rad51-ssDNA filament dynamics. *Methods Mol. Biol.* **2281**, 193–207 (2021).

Acknowledgements We thank members of the laboratories of P.S., E.C.G. and S.K.O. for discussions. Research reported in this publication was supported by NIH grants R01 GM115568 and R01 GM128731 (S.K.O.); R01 CA168635, R01 ES007061, P01 CA92584 and R35 CA241801 (P.S.); R00 GM140264 (E.V.W.); R01 CA221858 and R35 GM118026 (E.C.G.); R01 GM141091 and RSG-22-721675-01-DMC (W.Z.); R01 CA246807 and R01 CA258381 (S.B.); R01 GM136717, R01 CA23728, R01 CA188347 and Congressionally Directed Medical Research Programs BC191160 (A.V.M.); R50 CA265315 (Y.K.); R35 CA253174 (M.J.); R01 ES030335, ES031796 and the Department of Defense BC201356 (K.A.B.); and R01 CA139429 and Cancer Prevention and Research Institute of Texas RP220269 (R.H.). P.S. is the holder of the Robert A. Welch

Distinguished Chair in Chemistry (AQ-0012) and the recipient of a CPRIT REI Award (RR180029). A.V.M. is the holder of the Joe R. and Teresa Lozano Long Chair in Cancer Research and is the recipient of a CPRIT REI Award (RR210023). S.K.O. is the recipient of a CPRIT Rising Star Award (RR200030), and E.V.W. is the recipient of a CPRIT Recruitment of First Time Tenure Track Faculty Award (RR220068). E.C.G. is a recipient of a Wellcome Trust Collaborative Award in Science (206292/D/17/Z). The cryo-EM data used for the BCDX2 reconstruction were collected at the UT Health San Antonio Cryo-EM Facility on a Glacios transmission electron microscope equipped with a Falcon IV camera and a Selectris energy filter purchased with the support of University of Texas STARs awards 402-1288 (P.S.) and 402-1317 (S.K.O.). We thank A. Brilot for assistance screening cryo-EM grids at the University of Texas at Austin Sauer Structural Biology Laboratory (RRID:SCR_022951). We thank B. Hunter at the UT Health San Antonio Electron Microscopy Laboratory of South Texas Reference Laboratories, Department of Pathology and Laboratory Medicine, for assistance with negative-stain EM. The SPR assay was carried out in the Center for Innovative Drug Discovery and the Mays Cancer Center Drug Discovery and Structural Biology Shared Resource supported by CPRIT Core Facility Award RP160844 (D.Z.) and NIH-NCI P30 CA054174 (S.K.O. and D.Z.), respectively. The content of this study is solely the responsibility of the authors and does not necessarily represent the official views of the NIH.

Author contributions Protein purification was conducted by Y.R. and H.K. Structural experiments and analysis were conducted by L.J., E.A.R., E.V.W. and S.K.O. Y.R. conducted biochemical, mass photometry and negative-stain EM assays. S.Z. conducted SPR assays. A.M. conducted single-molecule experiments. K.A.B., M.J., Y.K., R.H., A.B.T., S.B., A.V.M., W.Z. and D.Z. assisted with experimental design and data interpretation. The figures and manuscript were prepared by Y.R., L.J., A.M., Y.K., E.V.W., E.C.G., P.S. and S.K.O., with input from all authors.

Competing interests The authors declare no competing interests.

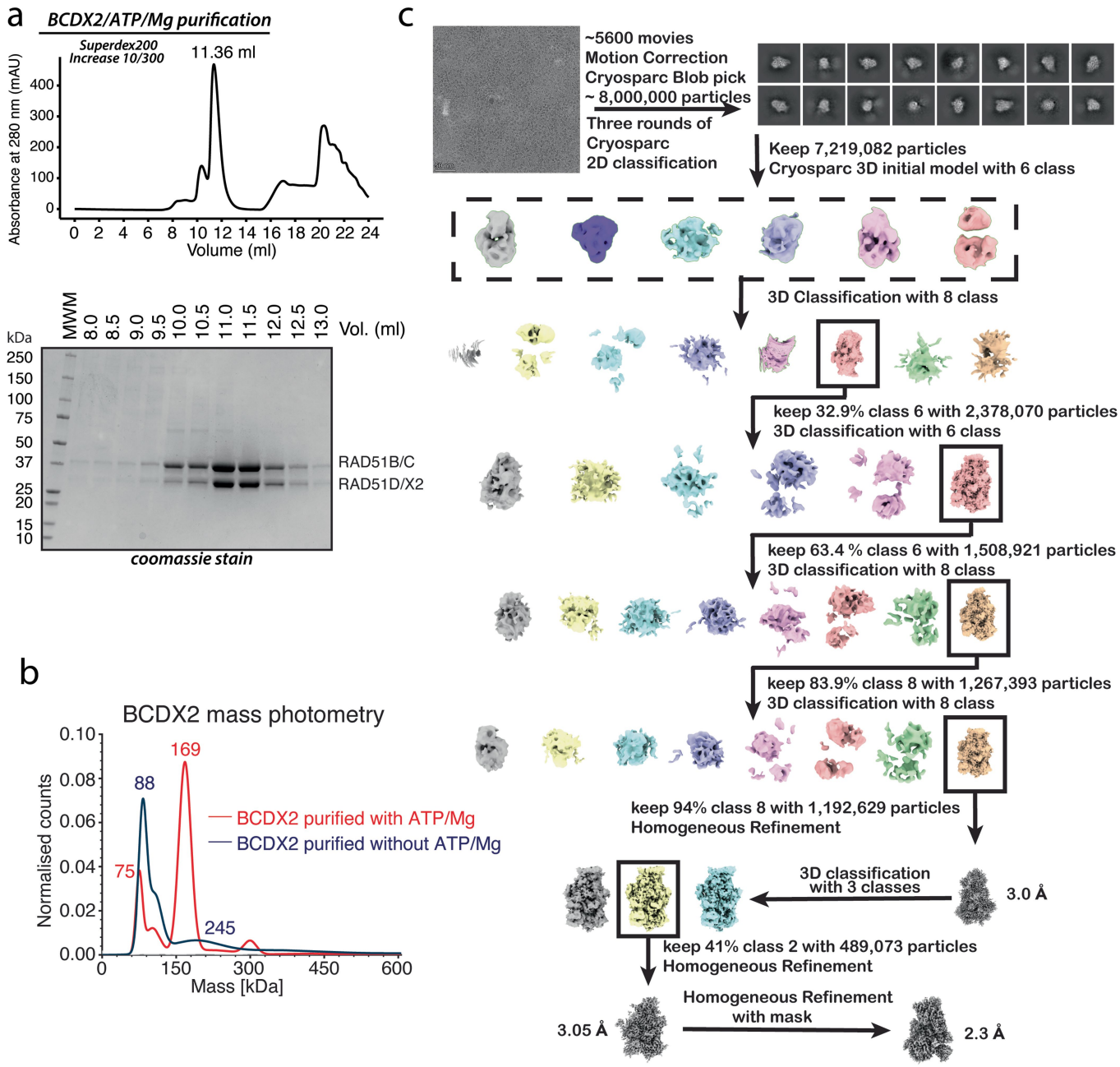
Additional information

Supplementary information The online version contains supplementary material available at https://doi.org/10.1038/s41586-023-06219-w.

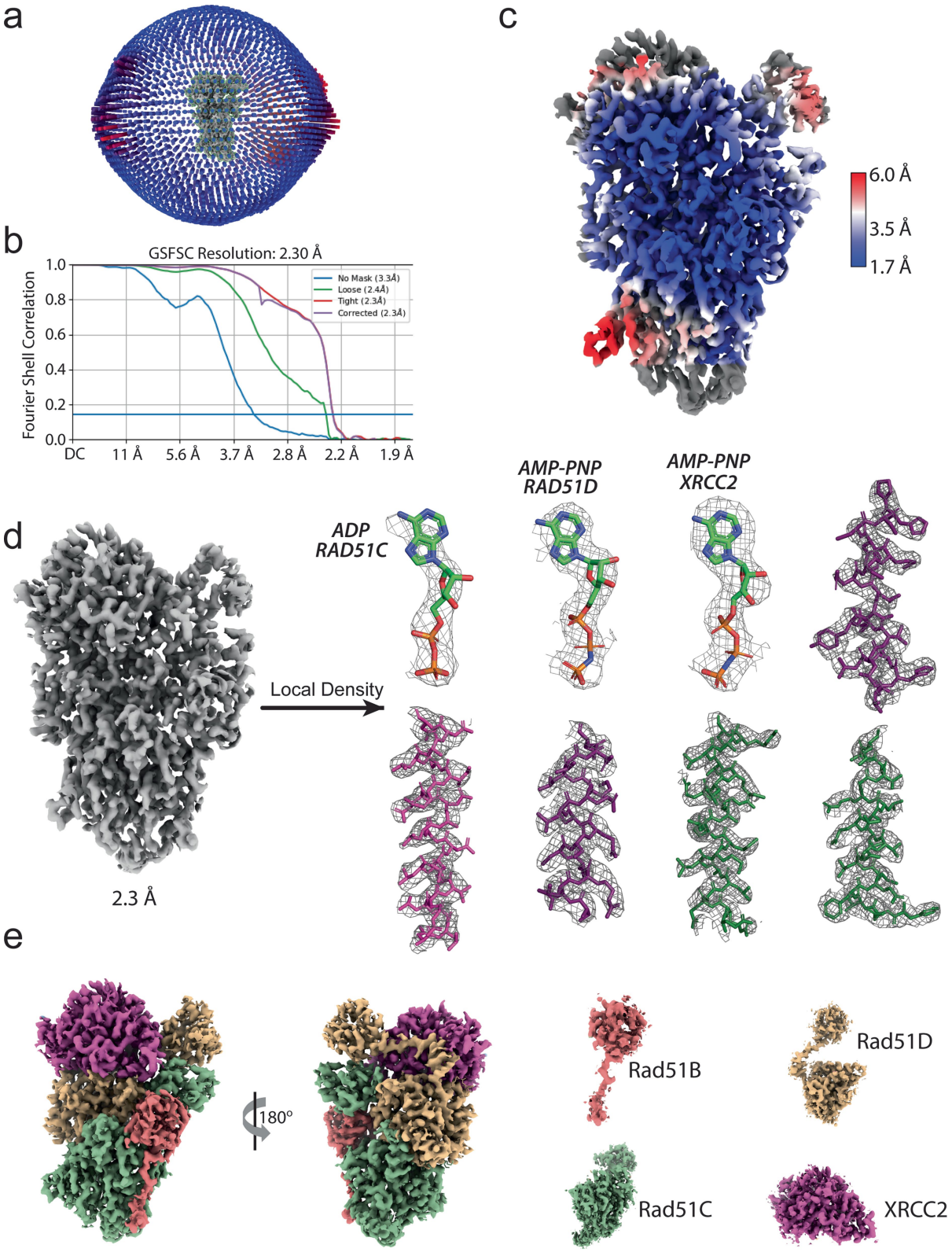
Correspondence and requests for materials should be addressed to Eric C. Greene, Patrick Sung or Shaun K. Olsen.

Peer review information *Nature* thanks the anonymous reviewers for their contribution to the peer review of this work. Peer reviewer reports are available.

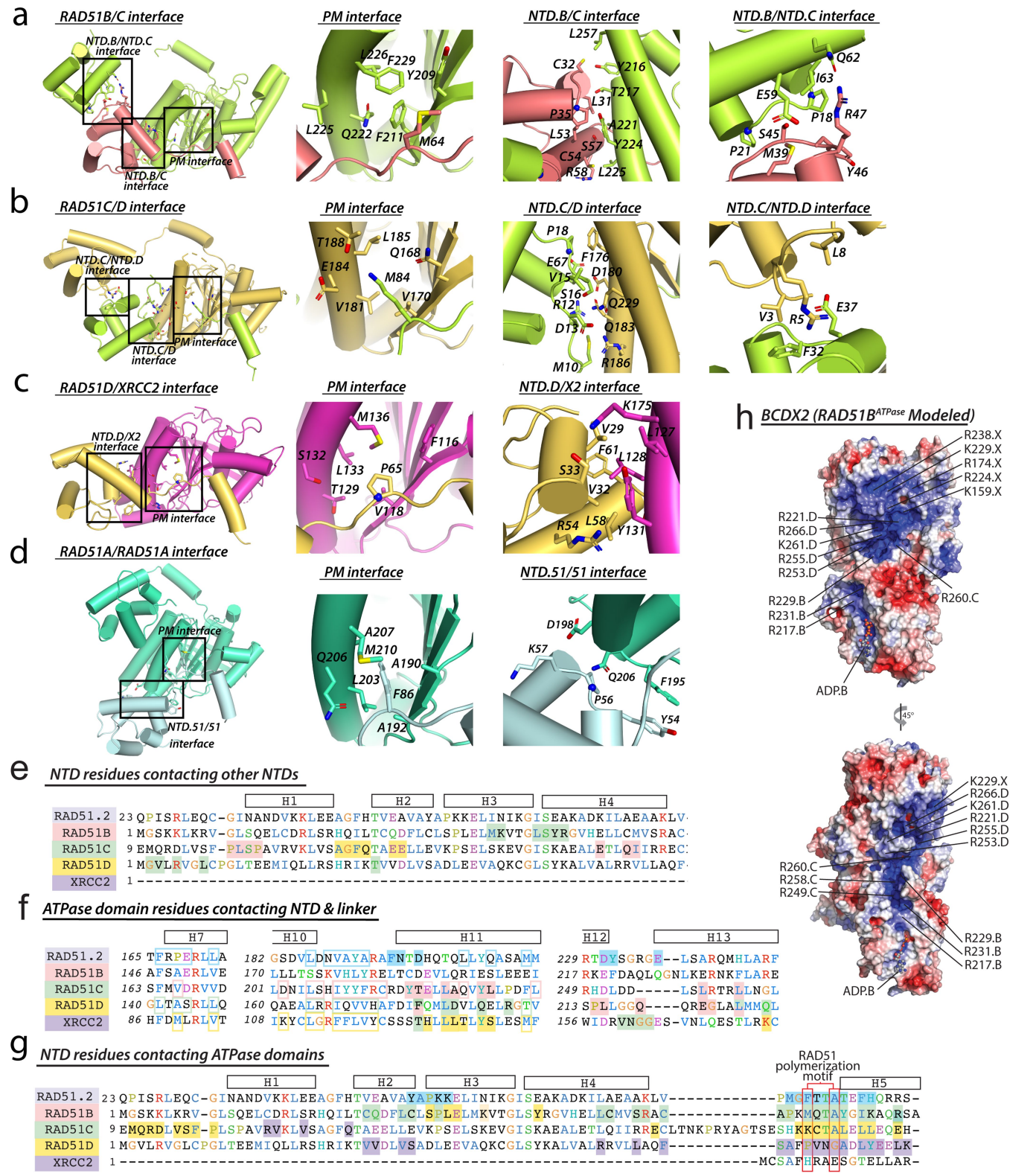
Reprints and permissions information is available at http://www.nature.com/reprints.



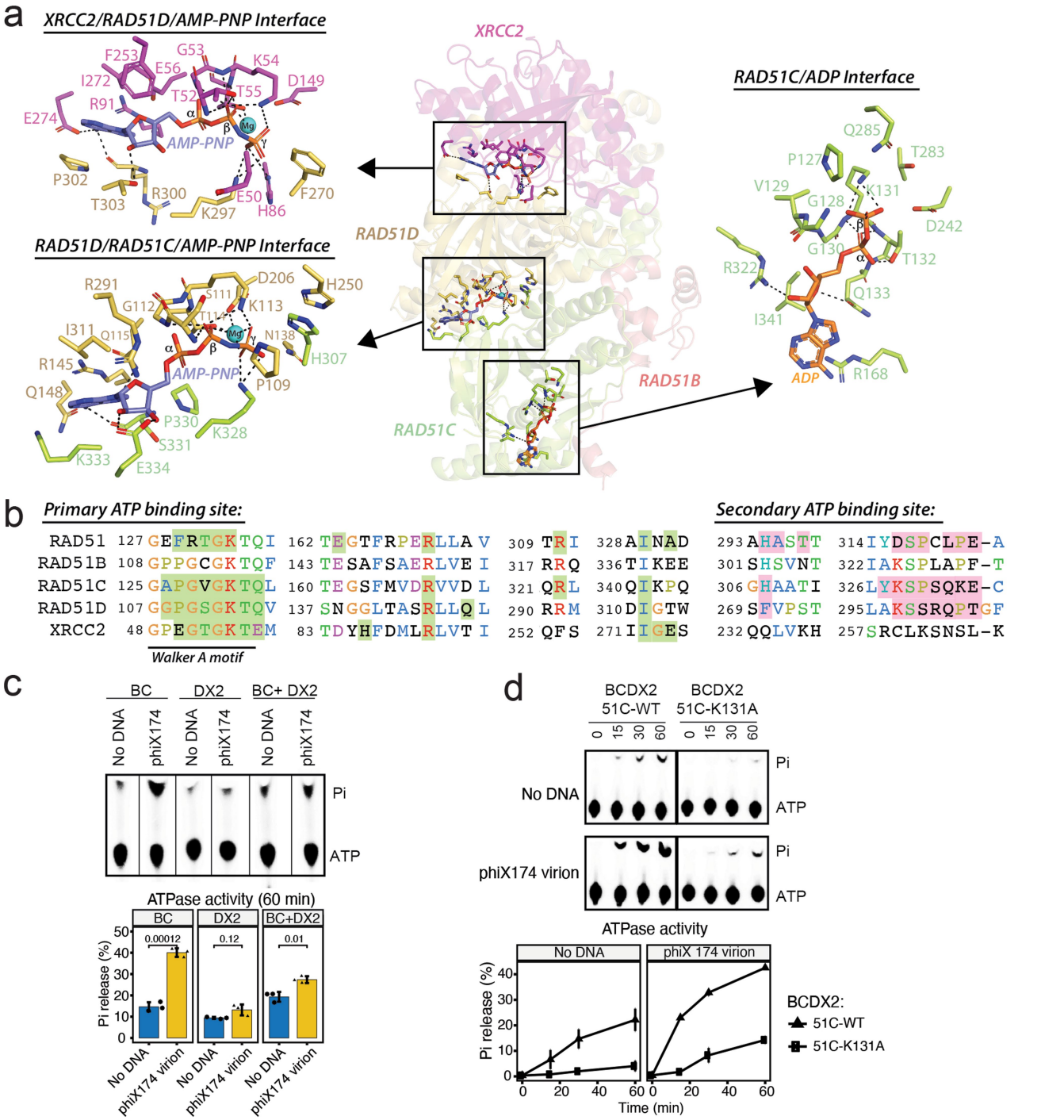
Extended Data Fig. 1 | BCDX2 reconstitution and cryo-EM data processing flowchart for apo structure. a, Chromatogram of an analytical gel filtration of the BCDX2 complex in the presence of ATP/Mg^{2+} on a Superdex200 Increase 10/300 column expressed and purified as described in the *Methods* (*top*). Coomassie-stained SDS-PAGE gel of the indicated fractions representing multiple replicates (*bottom*). **b**, Mass photometry analysis of the BCDX2 complex purified in the presence (red) and absence (blue) of ATP and Mg^{2+}. Both samples were rapidly diluted into PBS immediately prior to data acquisition. **c**, Auto-picked particles were first sorted by three rounds of 2D classification, six initial models were made first then followed by four rounds of heterogenous refinement. A final step of stringent heterogenous refinement and tight mask homogeneous refinement led to a final higher resolution map. All data analysis were performed using Cryosparc v3.3.1.



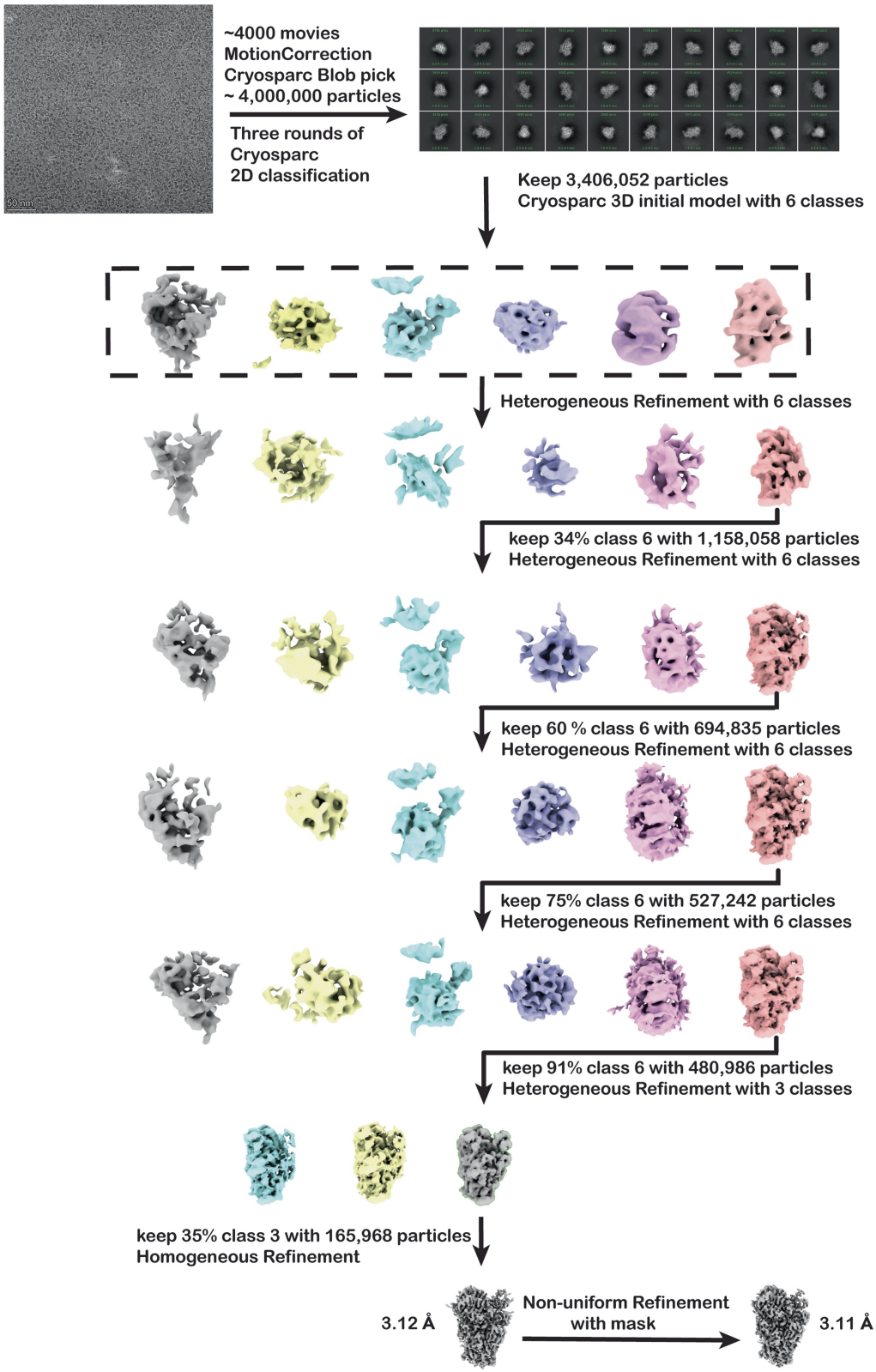
Extended Data Fig. 2 | Quality of the apo BCDX2 complex cryo-EM reconstruction. a, The final Euler angle distribution of particles used for 3D refinement. **b**, Fourier Shell Correlation (FSC) plot from two half maps, with an overall resolution of 2.3 Å as determined at 0.143 criterion. **c**, Local resolution map color-coded from lower (red) to higher resolution (blue). **d**, Overall map (*left*) and detailed views of local cryo-EM density for selected regions of the BCDX2 complex (*right*). **e**, Cryo-EM map of the BCDX2 complex with two views related by a 180° rotation about the y-axis (*left*). Maps of the individual subunits are shown to the *right* with RAD51B (pink), RAD51C (green), RAD51D (yellow), XRCC2 (purple).



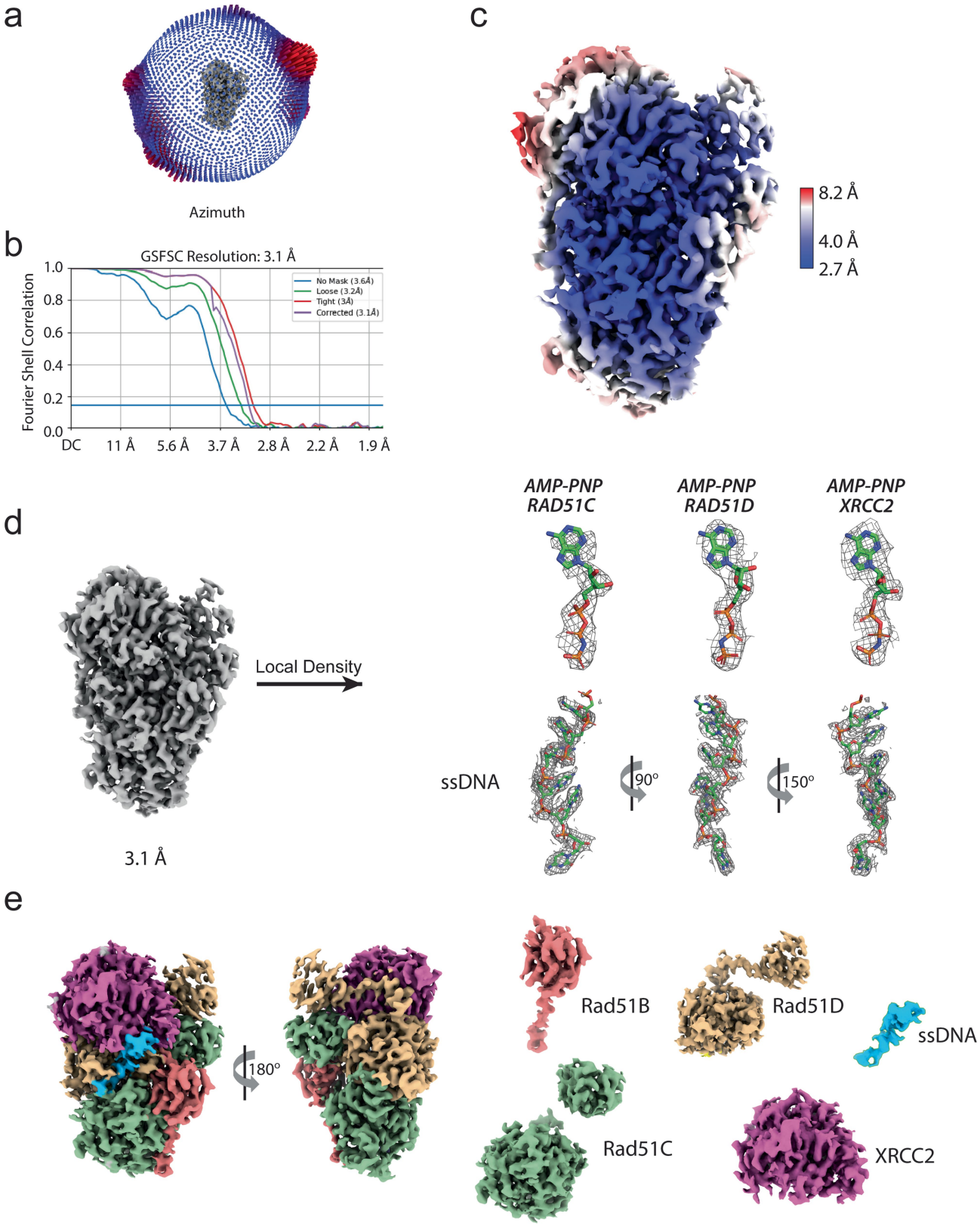
Extended Data Fig. 3 | Subunit-subunit interaction networks within the BCDX2 complex. a, Cartoon representation of the indicated RAD51B/RAD51C interface with residues involved in intermolecular interaction shown as sticks. An overview of the complex is shown on the *left* with magnified views of the indicated interfaces presented in the three *right* panels. **b**–**d**, The indicated complexes are presented as in *panel a* with RAD51C/RAD51D (*panel b*), RAD51D/XRCC2 (*panel c*), and RAD51/RAD51 from the presynaptic filament (PDB: 7EJC) (*panel d*). **e**–**g**, Structure-based sequence alignment of the indicated proteins. Residue numbers to the left of the sequence, secondary structure elements (RAD51 as a reference) are shown on top of the sequence. Contacts to RAD51 (shaded cyan), RAD51B (salmon), RAD51C (green), RAD51D (gold), and XRCC2 (magenta). In *panel g*, solid shade indicates ATPase domain contacts to the NTD and boxed shaded regions indicate contacts to the linker. **h**, Surface electrostatic representation of the complete BCDX2 complex with the ATPase domain of RAD51B modeled using AlphaFold and residues comprising the basic patch which serves as the putative nucleic acid binding site labeled.



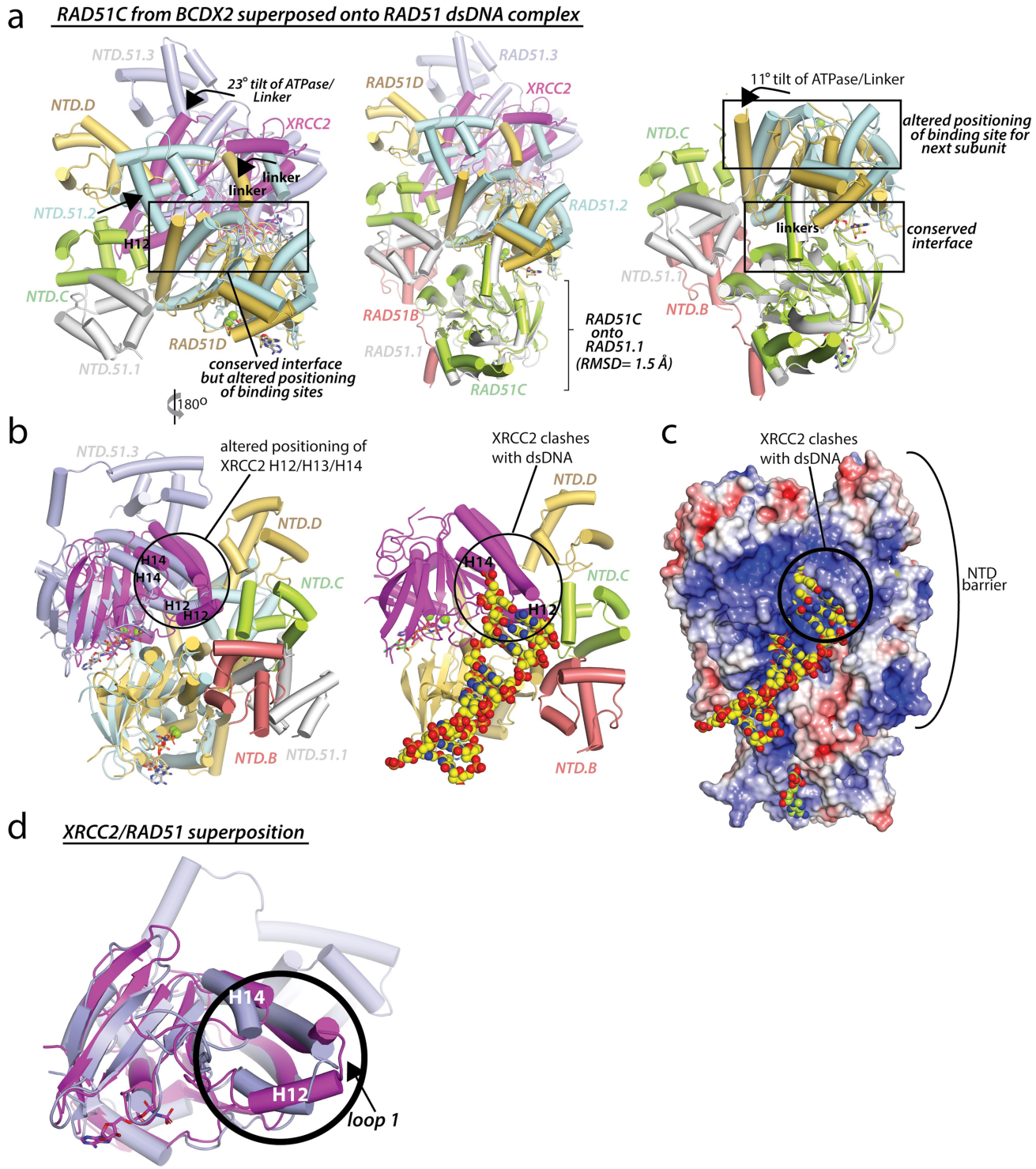
Extended Data Fig. 4 | Structural features and functional analysis of BCDX2 subunit active sites. a, Overview of the BCDX2 structure shown as a semitransparent cartoon with. ATP and BCDX2 residues contacting ATP are shown as solid sticks (*center*). Active sites are boxed. Magnified views of BCDX2 active sites are shown in the left and right panels. **b**, Structure-based sequence alignment of ATP binding sites of BCDX2 subunits and RAD51. Nucleotides are buried at the interface between subunits and the primary ATP binding site is defined as the subunit with its Walker A motif contacting ATP while the secondary ATP binding site is defined as the subunit contributing interacting residues on the other side of ATP. Interacting residues from primary and secondary ATP binding sites are colored green and pink, respectively. RAD51 (PDB: 7EJC) is shown for reference. **c**, ATPase assays of 1μM indicated BCDX2 variants in the presence or absence of ssDNA after 60 min incubation. Pi indicates released inorganic phosphate after hydrolysis. The histograms show results from three independent experiments, data are presented as mean values ±SD and *p*-values for the significance of differences in mean values were calculated by the two-sided t-test are indicated. **d**. ATP hydrolysis with 1 μM WT and indicated mutant BCDX2 complexes with or without ssDNA were assessed for indicated time points and measurements for three independent experiments were plotted as mean values ±SD. ATPase images in *panels c and d* were derived from same experiment and processed in parallel.



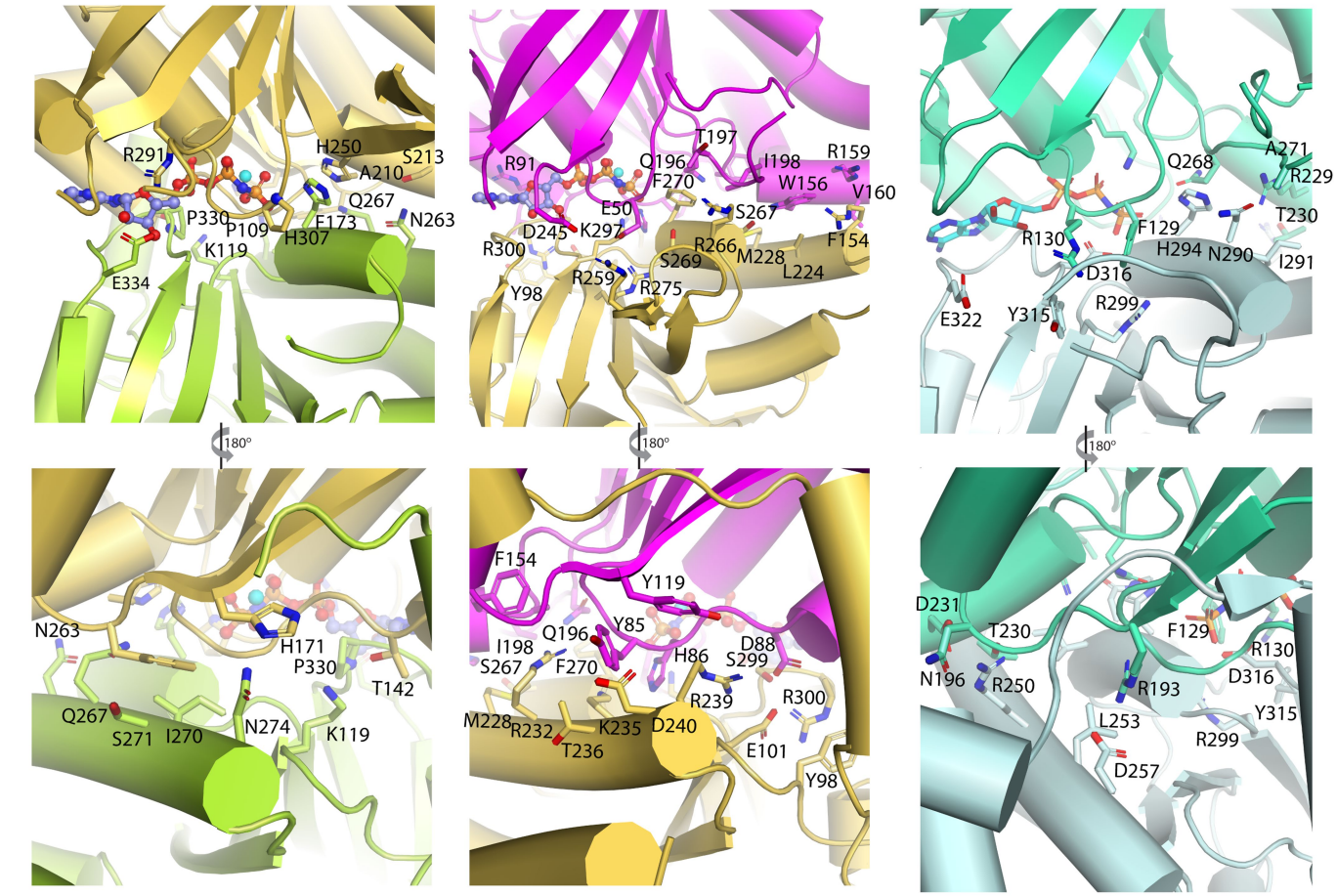
Extended Data Fig. 5 | Cryo-EM data processing flowchart for the BCDX2/ssDNA structure. Auto-picked particles were first sorted by three rounds of 2D classification. Next, six initial models were generated, followed by four rounds of heterogenous refinement. A subsequent step of stringent heterogenous refinement and tight mask homogeneous refinement of class 3 resulted in a map with 3.12 Å resolution. A final non-uniform refinement yields final map of 3.11Å resolution. All data processing was performed using Cryosparc v3.3.1.



Extended Data Fig. 6 | Quality of the BCDX2-ssDNA complex cryo-EM reconstruction. a, The final Euler angle distribution of particles used for 3D refinement. **b**, Fourier Shell Correlation (FSC) plot from two half maps, with an overall resolution of 3.1 Å as determined at 0.143 criterion. **c**, Local resolution map color-coded from lower (red) to higher resolution (blue). **d**, Overall map (*left*) and detailed views of local cryo-EM density for AMP-PNP and ssDNA from the BCDX2/ssDNA structure (*right*). **e**, Cryo-EM map of the BCDX2 complex with two views related by a 180° rotation about the y-axis (*left*). Maps of the individual subunits are shown to the *right* with Rad51B (pink), Rad51C (green), Rad51D (yellow), XRCC2 (purple), ssDNA (cyan).



Extended Data Fig. 7 | A potential mechanism for the ssDNA binding specificity of BCDX2. a, RAD51C from BCDX2 was superposed onto RAD51 from the RAD51/ssDNA postsynaptic structure (PDB: 7EJE). Three subunits from the RAD51 filament are presented. An overview of the superposition is shown in the center panel, while magnified views of the RAD51C/RAD51D and RAD51D/XRCC2 subcomplexes are shown to the *right* and *left*, respectively. **b**, Magnified view of the RAD51D/XRCC2 module from panel a, rotated 180 degrees about the y-axis (*left*). *Right*, dsDNA from the RAD51/dsDNA postsynaptic complex is shown as spheres with the RAD51 structure omitted for clarity. Note clashes between dsDNA and XRCC2 due to 11 and 23 degree tilts at the RAD51C/RAD51D and RAD51D/XRCC2 interfaces, respectively, compared to RAD51. **c**, Surface electrostatic representation of the BCDX2 complex with dsDNA from the superposition presented in *panels a and b*. Note clashes between dsDNA and XRCC2 and close proximity of the NTDs of BCDX2 to dsDNA. **d**, Superposition of XRCC2 onto RAD51. Note structural differences in length and conformation of the loop 1 region including helices H12 and H14, which clash with dsDNA in the model.



d

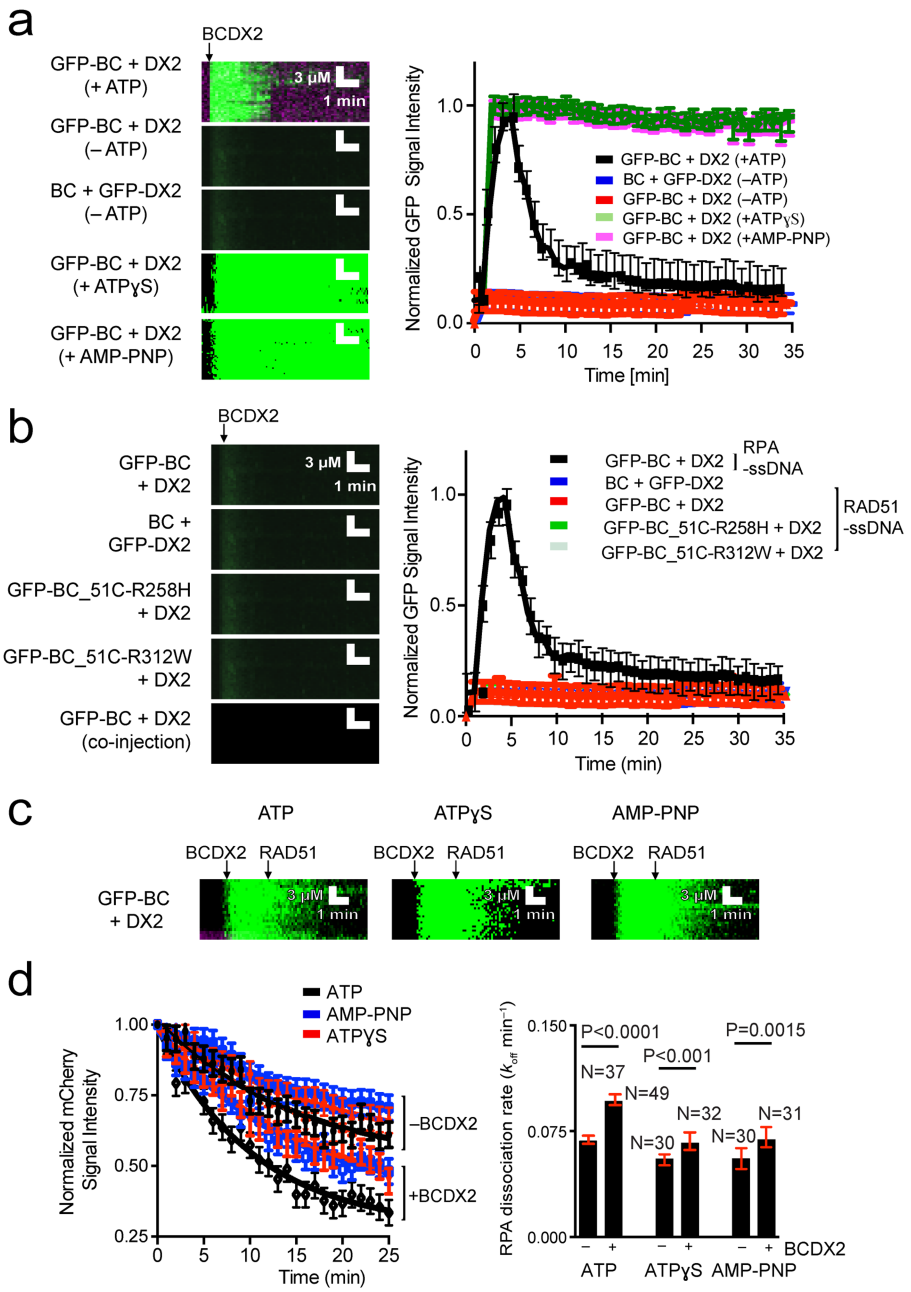
Residues involved in ATPase domain/ATPase domain interactions

RAD51.2	117	IET-GSITEMFGEFRTGKTQI	161	DTEGTFRPERLLAV	192	ARAFN
RAD51B	98	VAC-GSLTEITGPPGCGKTQF	142	DTESAFSAERLVEI	180	YRELT
RAD51C	115	VPL-MKTTEICGAPGVGKTQL	159	DTEGSFMVDRVVDL	211	FRCRD
RAD51D	97	LYT-GEVTEIVGGPGSGKTQV	136	DSNGGLTASRLLQL	170	VHAFD
XRCC2	37	SPVHGDILEFHGPEGTGKTEM	82	DTDYHFDMLRLVTI	118	VYCSS

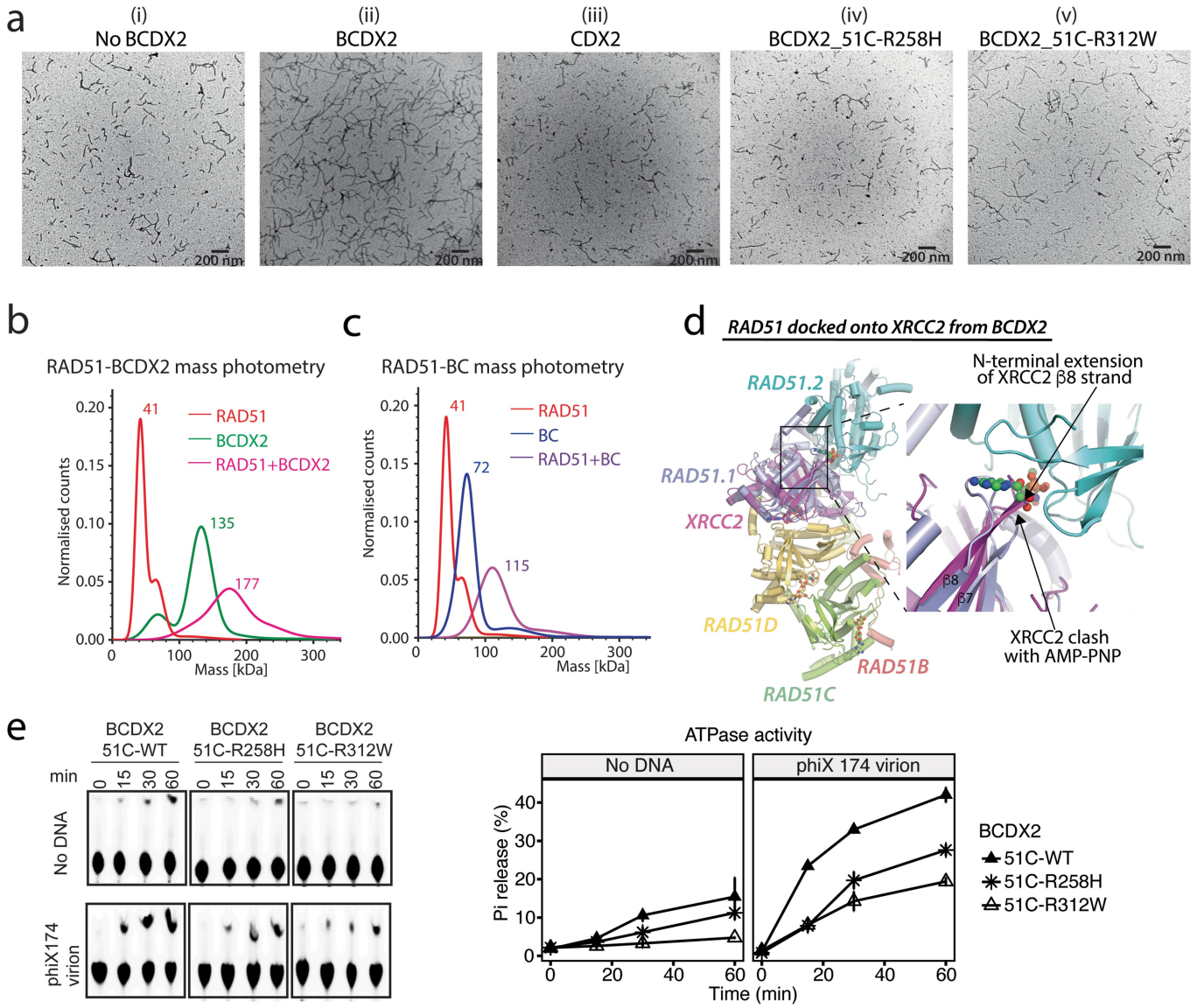
RAD51.2	225	TALYRTDYSGRGE--LSARQMHLARFLRMLLRLADEFGVAVVITNQVVAQVDGAAM
RAD51B	213	ASVVRKEFDAQLQGNLKERNKFLAREASSLKYLAEEFSIPVILTNQITTHLSGALA
RAD51C	245	AFPFRHDLDD-----LSLRTRLLNGLAQQMISLANNHRLAVILTNQMTTKIDRNQA
RAD51D	209	TAVVSPLLGGQ----QREGLALMMQLARELKTLARDLGMAVVVTNHITRDRDSGR-
XRCC2	152	SAFYWIDRVNGGES-VNLQESTLRKCSQCLEKLVNDYRLVLFATTQTIMQKASSSS

RAD51.2	289	GNIIAHASTTRLYLRKGR-----GETRICKIYDSPCLPE-
RAD51B	297	GNTWSHSVNTRLILQYLD-----SERRQILIAKSPLAPF-
RAD51C	302	GESWGHAATIRLIFHW-D-----RKQRLATLYKSPSQKE-
RAD51D	265	GRSWSFVPSTRILLDTIEGAGASGGRRMACLAKSSRQPTG
XRCC2	228	CKAWQQLVKHRMFFSKQD-DSQSSNQFSLVSRCLKSNSL-

Extended Data Fig. 8 | Comparison of ATPase/ATPase domain interactions in BCDX2 and RAD51. a–**c**, Analysis of the amino acid interaction networks at the ATPase/ATPase interfaces of the RAD51C/RAD51D (*panel a*), and RAD51D/XRCC2 (*panel b*) subcomplexes of BCDX2, and RAD51/RAD51 from the RAD51/ssDNA presynaptic filament complex (PDB:7EJC) (*panel c*). Structures are shown as cartoon representations with residues involved in intermolecular interactions shown as sticks. Two views of the complexes related by a 180 degree rotation about the y-axis are shown in the top and bottom panels. **d**, Structure-based sequence alignment highlighting ATPase domain/ATPase domain interactions at the interfaces highlighted in *panels a-c*. Residues are colored by the subunit to which they interact: RAD51C (green), RAD51D (gold), XRCC2 (magenta), and RAD51 (cyan). The ATPase domain of RAD51B is not visible in the BCDX2 structure but is included in the sequence alignment for comparison.



Extended Data Fig. 9 | Characterization of BCDX2 recombination mediator activity. a, Representative kymographs of single ssDNA molecules (*left panel*) showing GFP-BC + DX2 plus ATP (reproduced from Fig. 4a, for comparison), GFP-BC + DX2 minus ATP, BC + GFP-DX2 minus ATP, GFP-BC + DX2 plus ATPγS and GFP-BC + DX2 (green channel; 10 nM each protein complex) plus AMP-PNP (2.5 mM ATP or ATP analogue) binding to mCherry-RPA-ssDNA (red channel). The graph (*right panel*) shows quantification of GFP-BCDX2 binding to the mCherry-RPA-ssDNA. The graph for GFP-BC + DX2 was reproduced from Fig. 4b for comparison. Data are represented as mean normalized GFP signal intensity; error bars represent 95% CI. Data were derived from three flow cells per reaction condition. **b**, Representative kymographs of single ssDNA molecules (*left panel*) showing GFP-BC + DX2 (reproduced from Fig. 4a, for comparison), GFP-BC-R258H + DX2, GFP-BC-R312W + DX2 (10 nM each protein complex) in the presence of 2.5 mM ATP binding to and dissociating from a mCherry-RPA-ssDNA. The graph (*right panel*) shows quantification of GFP-BCDX2 binding to the mCherry-RPA-ssDNA. The graph for GFP-BC + DX2 (+ATP) was reproduced from Fig. 4b for comparison. Data are represented as mean normalized GFP signal intensity; error bars represent 95% CI. Data were derived using three flow cells per reaction condition. **c**, Representative kymographs of single RPA-ssDNA molecules showing the behavior of GFP-BC+DX2 in reactions with ATP (*left kymograph*), ATPγS (*center kymograph*) and AMP-PNP (*right kymograph*) during RAD51 filament assembly. **d**, Quantification of mCherry-RPA dissociation during RAD51 filament assembly in the presence and absence of BCDX2 (*left panel*), as indicated. Data represented the mean normalized mCherry signal intensity. Data were derived using three flow cells per reaction condition. Calculated rates for RPA-mCherry dissociation from ssDNA during RAD51 filament assembly (*right panel*). Error bars represent 95% CI. n = 3 flow cells per data set; *p*-values were calculated by unpaired t-test (two-sided).



Extended Data Fig. 10 | Biophysical and biochemical characterization of BCDX2 functions. a, Representative micrographs depicting RAD51 nucleoprotein filaments seen by negative stain electron microscopy in absence or presence of BCDX2, CDX2 and BCDX2 with RAD51C mutants R258H and R312W. Data represent at least 40 electron micrographs for each sample captured in two independent experiments. **b,c**, Mass photometry analysis of the RAD51 interactions with (*panel b*) BCDX2 complex and (*panel c*) BC subcomplex in the presence of ATP/Mg^{2+}. Plots representing molecular mass profiles RAD51, BCDX2, BC alone and RAD51 when mixed with BCDX2 or BC are differently color coded and molecular mass of most prominent peak in each sample is indicated. **d**, A two protomer fragment of the RAD51 presynaptic filament (RAD51.1 in slate and RAD51.2 in cyan) were superimposed onto the XRCC2 subunit of XRCC2 subunit of the BCDX2 complex. The overall model is shown in the *left panel* and a magnified view of the ATP binding site at the interface between XRCC2 and RAD51.1 is shown in the *right panel*. Note that the β8 strand of XRCC2 is extended by several residues and the loop between β7 and β8 adops a significantly different conformation from RAD51 which clashes with ATP in the model. **e**, ATP hydrolysis with 1 μM WT and indicated mutant BCDX2 complexes with or without ssDNA were assessed for indicated time points and measurements for three independent experiments were plotted as mean values ±SD. ATPase images were derived from same experiment and processed in parallel.

Extended Data Table 1 | Cryo-EM data collection, refinement, and validation statistics

	apo BCDX2 (EMDB-28961) (PDB 8FAZ)	BCDX2-ssDNA (EMDB-29917) (PDB 8GBJ)
Data collection and processing		
Magnification	130K	130K
Voltage (kV)	200	200
Electron exposure (e–/Å^2)	51	52
Defocus range (μm)	0.8- 2.0	0.8 -2.0
Pixel size (Å)	0.87	0.87
Symmetry imposed	C1	C1
Initial particle images (no.)	7219082	3406052
Final particle images (no.)	489073	165968
Map resolution (Å)	2.3	3.1
FSC threshold 0.143 (Å)		
Map resolution range (Å)	2.3-3.3	3.1-3.6
Refinement		
Initial model used (PDB code)	N/A AlphaFold	N/A AlphaFold
Model resolution (Å)	2.3	3.1
FSC threshold 0.143 (Å)		
Model resolution range (Å)	2.3-3.3	3.1-3.6
Map sharpening *B* factor (Å^2)	52.2	110.2
Model composition		
Non-hydrogen atoms	0	0
Protein residues	7280	7468
Ligands	91	93
Nucleotide	0a	118a
B factors (Å^2)		
Protein	67.8	48.6
Ligand	61.8	18.3
Nucleotide	N/A	49.8
R.m.s. deviations		
Bond lengths (Å)	0.002	0.004
Bond angles (°)	0.444	0.633
Validation		
MolProbity score	1.6	1.7
Clashscore	10.4	14.6
Poor rotamers (%)	1.98	0.37
Ramachandran plot		
Favored (%)	97.6	97.6
Allowed (%)	2.4	2.4
Disallowed (%)	0	0

Extended Data Table 2 | Structural similarity and SPR interaction between RAD51 and BCDX2

ATPase Domains:

Protein 1	Protein 2	Superposition Length	RMSD (Å)	% Identity	% Similarity
RAD51	RAD51C	218	1.49	29	43
RAD51	RAD51D	220	1.86	25	41
RAD51	XRCC2	225	2.68	21	34
RAD51C	RAD51D	214	2.05	23	41
RAD51C	XRCC2	221	3.06	20	33
RAD51D	XRCC2	220	2.59	16	36

NTDs*:

Protein 1	Protein 2	Superposition Length	RMSD (Å)	% Identity	% Similarity
RAD51	RAD51C	57	1.74	25	40
RAD51	RAD51D	61	2.09	13	28
RAD51C	RAD51D	56	2.08	15	41

SPR analysis of RAD51 and BCDX2 interaction

Analyte	Ligand	ka(1/Ms)	kd(1/s)	KD(M)
RAD51	BCDX2	3.09×10^{5}	7.91×10^{-4}	2.56×10^{-9}
RAD51	BC	3.23×10^{5}	2.78×10^{-4}	8.61×10^{-10}
RAD51	DX2	N/A	N/A	N/A

*XRCC2 lacks an NTD
N/A: not available. The data could not be reasonably fit into a model
ka: association rate constant
kd: dissociation rate constant
KD: dissociation equilibrium constant
Note: Heterogeneous model was used for data fitting, and the tight binding stage was used as the interaction between the analyte and ligand listed.

nature portfolio

Corresponding author(s): Eric C. Greene, Patrick Sung, Shaun K. Olsen

Last updated by author(s): Apr 30, 2023

Reporting Summary

Nature Portfolio wishes to improve the reproducibility of the work that we publish. This form provides structure for consistency and transparency in reporting. For further information on Nature Portfolio policies, see our Editorial Policies and the Editorial Policy Checklist.

Statistics

For all statistical analyses, confirm that the following items are present in the figure legend, table legend, main text, or Methods section.

n/a	Confirmed	
☐	☒	The exact sample size (*n*) for each experimental group/condition, given as a discrete number and unit of measurement
☐	☒	A statement on whether measurements were taken from distinct samples or whether the same sample was measured repeatedly
☐	☒	The statistical test(s) used AND whether they are one- or two-sided *Only common tests should be described solely by name; describe more complex techniques in the Methods section.*
☐	☒	A description of all covariates tested
☐	☒	A description of any assumptions or corrections, such as tests of normality and adjustment for multiple comparisons
☐	☒	A full description of the statistical parameters including central tendency (e.g. means) or other basic estimates (e.g. regression coefficient) AND variation (e.g. standard deviation) or associated estimates of uncertainty (e.g. confidence intervals)
☐	☒	For null hypothesis testing, the test statistic (e.g. *F*, *t*, *r*) with confidence intervals, effect sizes, degrees of freedom and *P* value noted *Give P values as exact values whenever suitable.*
☒	☐	For Bayesian analysis, information on the choice of priors and Markov chain Monte Carlo settings
☒	☐	For hierarchical and complex designs, identification of the appropriate level for tests and full reporting of outcomes
☒	☐	Estimates of effect sizes (e.g. Cohen's *d*, Pearson's *r*), indicating how they were calculated

Our web collection on statistics for biologists contains articles on many of the points above.

Software and code

Policy information about availability of computer code

Data collection	SM data were collected using NIS-elements Version 5.11 (Nikon). Cryo-EM data was collected on Glacios microscope with Falcon4 camera and Seletrics energy filter at UTHSCSA
Data analysis	SM image analysis was performed using Open-source image processing software ImageJ v2.90/153t. Data analysis and graphs were plotted using GraphPad Prism version 8.4.3 (686). ATPase, DNA binding and negative staining data were plotted using R (3.6.1) package ggpubr. Cryo-EM data analysis were performed on open source softwares, including Cryosparc v3.3.1, Alphafold2, UCSF ChimeraX v1.4, COOT v0.9.3, PHENIX V1.19.1-4122-000, PyMOL v2.0

For manuscripts utilizing custom algorithms or software that are central to the research but not yet described in published literature, software must be made available to editors and reviewers. We strongly encourage code deposition in a community repository (e.g. GitHub). See the Nature Portfolio guidelines for submitting code & software for further information.

Data

Policy information about availability of data

All manuscripts must include a data availability statement. This statement should provide the following information, where applicable:

- Accession codes, unique identifiers, or web links for publicly available datasets
- A description of any restrictions on data availability
- For clinical datasets or third party data, please ensure that the statement adheres to our policy

Atomic coordinates for apo BCDX2 and BCDX2/ssDNA complexes are deposited in the RCSB with accession codes 8FAZ and 8GBJ, respectively. The corresponding cryo-EM maps have been deposited into the Electron Microscopy Data Bank with accession numbers EMD-28961 (apo BCDX2) and EMD-29917 (BCDX2/ssDNA). Coordinates and cryo-EM maps for protein structures discussed or used in analyses are accessible at the RCSB. The structural data used from RCSB are listed below: PDB: 7EJC and PDB: 7EJE. Extended data is available for this paper.

Human research participants

Policy information about studies involving human research participants and Sex and Gender in Research.

Reporting on sex and gender	N/A
Population characteristics	N/A
Recruitment	N/A
Ethics oversight	N/A

Note that full information on the approval of the study protocol must also be provided in the manuscript.

Field-specific reporting

Please select the one below that is the best fit for your research. If you are not sure, read the appropriate sections before making your selection.

☒ Life sciences ☐ Behavioural & social sciences ☐ Ecological, evolutionary & environmental sciences

For a reference copy of the document with all sections, see nature.com/documents/nr-reporting-summary-flat.pdf

Life sciences study design

All studies must disclose on these points even when the disclosure is negative.

Sample size	For biochemistry, sample sizes were chosen based on our previous experience to obtain statistical significance and reproducibility. Exact sample sizes are included in the paper. For single molecule measurements, exact volume of the flow cell cannot be defined, proteins were injected in HR buffer in major excess to fill the entire flow cell.
Data exclusions	No data were excluded from any assays.
Replication	For biochemistry and single molecule measurements, all findings were repeated as indicated in the paper and all the replication attempts were successful. Single molecule data represents a minimum of three experimental replicates to ensure reproducibility.
Randomization	Randomization was not part of the study design. In vitro and single molecule assay samples were assigned to experimental in a non-biased way.
Blinding	Blinding was not part of the study design. This research involved molecular analysis of specific protein mutants and the researchers needed to make and characterize each mutant separately.

Reporting for specific materials, systems and methods

We require information from authors about some types of materials, experimental systems and methods used in many studies. Here, indicate whether each material, system or method listed is relevant to your study. If you are not sure if a list item applies to your research, read the appropriate section before selecting a response.

Materials & experimental systems

n/a	Involved in the study
☒	☐ Antibodies
☐	☒ Eukaryotic cell lines
☒	☐ Palaeontology and archaeology
☒	☐ Animals and other organisms
☒	☐ Clinical data
☒	☐ Dual use research of concern

Methods

n/a	Involved in the study
☒	☐ ChIP-seq
☒	☐ Flow cytometry
☒	☐ MRI-based neuroimaging

Eukaryotic cell lines

Policy information about cell lines and Sex and Gender in Research

Cell line source(s)	Sf9 cells (Spodoptera frugiperda, IPLB-Sf21-AE), Expression Systems 94001F. High Five Cells (Trichoplusia ni, BTI-Tn-5B1-4), Invitrogen™ B85502
Authentication	Cell lines were not authenticated, they are used for recombinant protein expression only.
Mycoplasma contamination	Cell lines were not tested for mycoplasma, they are used for recombinant protein expression only.
Commonly misidentified lines (See ICLAC register)	No commonly misidentified cell line was used